Hybrid Magnetic-Plasmonic Nanoparticle Probes for Multimodal Bioimaging

Cristina de la Encarnación[1,2], Elisa Lenzi[1,3], Malou Henriksen-Lacey[1,3], Beatriz Molina[1,4], Kellie Jenkinson[5], Ada Herrero[1,3], Lorena Colás[1], Pedro Ramos-Cabrer[1,6], Jhoan Toro-Mendoza[1], Iñaki Orue[7], Judith Langer[1,3], Sara Bals[5], Dorleta Jimenez de Aberasturi[1,3,6*], and Luis M. Liz-Marzán[1,3,6*]

[1] CIC biomaGUNE, Basque Research and Technology Alliance (BRTA), 20014, San Sebastián, Spain

[2] Department of Applied Chemistry, University of the Basque Country, 20018 Donostia-San Sebastián, Spain

[3] Centro de Investigación Biomédica en Red, Bioingeniería, Biomateriales y Nanomedicina (CIBER-BBN), 20014, San Sebastián, Spain

[4] Current address: Biobide Spain, Paseo Mikeletegi 56 Bajo, 20009 Donostia-San Sebastián, Spain

[5] EMAT and NANOlab Center of Excellence -University of Antwerp, 2020 Antwerp, Belgium

[6] Ikerbasque, Basque Foundation for Science, 48009 Bilbao, Spain

[7] SGIKER, Servicios Generales de Investigación, University of the Basque Country, 48940 Leioa, Spain

*Corresponding authors' email: djimenezdeaberasturi@cicbiomagune.es (D.J.d.A.); llizmarzan@cicbiomagune.es (L.M.L.-M.)

KEYWORDS

Multimodal bioimaging; hybrid nanoparticles; magnetic-plasmonic; SERS; MRI; Fluorescence imaging.

ABSTRACT

Multimodal contrast agents, which take advantage of different imaging modalities, have emerged as an interesting approach to overcome the technical limitations of individual techniques. We developed hybrid nanoparticles comprising an iron oxide core and an outer gold spiky layer, stabilized by a biocompatible polymeric shell. The combined magnetic and optical properties of the different components provide the required functionalities for magnetic resonance imaging (MRI), surface-enhanced Raman scattering (SERS), and fluorescence imaging. The fabrication of such hybrid nanoprobes comprised the adsorption of small gold nanoparticles onto pre-made iron oxide cores, followed by controlled growth of spiky gold shells. The gold layer thickness and branching degree (tip sharpness) can be controlled by modifying both the density of Au nanoparticle seeds on the iron oxide cores and the subsequent nanostar growth conditions. We additionally demonstrated the performance of these hybrid multifunctional nanoparticles as multimodal contrast agents for correlative imaging of *in vitro* cell models and *ex vivo* tissues.

INTRODUCTION

Early disease diagnosis is essential to increasing the chances of successful treatment. In this regard, advances in minimally invasive imaging techniques, from the single cell to the whole-body level, are essential in biomedicine.[1] However, one realistic concern is that a single imaging technique does not provide sufficient information for a precise diagnosis, and thus multimodal imaging techniques should provide advantages over each individual modality on its own.[2,3]

Most bioimaging techniques require the use of molecular or nanoparticulate contrast agents to improve the visualization of detailed features in tissues,[4] or to selectively recognize a specific component of particular relevance to the final diagnosis, for example, regions with inflammation or cancerous cells.[5] In particular, gold NPs (AuNPs) have shown great potential in the detection, diagnosis, and/or treatment of diseases.[6-8] AuNPs feature excellent plasmonic properties related to the interaction of their conduction electrons with incident light, yielding localized surface plasmon resonances (LSPRs). Therefore, AuNPs act as antennas for light, driving the amplification of the Raman signal of molecules in close proximity to their surface, a phenomenon known as surface-enhanced Raman scattering (SERS).[9] The anisotropic and pointed nature of Au nanostars (AuNSs) has been shown to render them excellent Raman enhancers, thanks to the particularly efficient electromagnetic field enhancement at their tips, which results in intrinsic hot spots. Consequently, AuNSs combined with Raman reporters (RaRs, i.e., molecules of high Raman cross section with well-defined characteristic vibrational fingerprints) have been extensively explored as labels for SERS bioimaging, both *in vitro* and *in vivo*.[10,11] In terms of clinically relevant imaging techniques, AuNSs have found application in photoacoustic, SERS, and computed tomography (CT) imaging,[12] but the diamagnetic nature of gold does not make it useful for more common nuclear magnetic resonance (NMR)-based

techniques, most often used for whole-body imaging in clinical settings. In particular, magnetic resonance imaging (MRI) plays an important role in the clinical diagnosis of many diseases because of its noninvasive nature and excellent safety profile.[13] Therefore, many attempts have been made toward combining Au with magnetic NPs, namely iron oxide NPs (IONPs), to conduct simultaneous imaging by MRI, CT and SERS, among other modalities.[14-16]

For example, the combination of MRI and SERS offers the fast operation and deep-tissue penetration of MRI to obtain a global picture of the tissue,[17] combined with the high sensitivity of SERS that allows more detailed structures to be resolved.[18] This multimodal imaging, however, requires the use of multifunctional NPs, which must be synthesized with accurate control over the various synthesis parameters. Most of the studies found in the literature focus on the fabrication of core-shell hybrid NPs comprising a magnetic core encapsulated by an Au-based plasmonic shell. This is partly due to the availability of simple and reliable synthesis methods for IONPs, such as co-precipitation or thermal decomposition,[19] as well as optimized protocols for gold encapsulation.[20-22] However, anisotropic NPs featuring spikes or edges that can act as hot spots for SERS are preferred for signal enhancement, especially in biological samples where high background values require strong SERS intensities. One such example is the synthesis of magnetic-plasmonic Janus NPs comprising a single magnetic core and a spiky gold region.[12] However, this system is restricted to magnetic cores of ~ 10 - 20 nm in diameter and is only partially covered by Au. In the present study, we prepared magnetic-plasmonic NPs by growing a spiky gold shell on pre-made multi-core iron oxide nanoflowers. Magnetic iron oxide nanoflowers comprise multiple crystallites and therefore show an improved magnetic response, as compared to single-core NPs of similar size. The reason is exchange coupling occurring among individual crystallites in multi-core systems due to the short distances between them, thus

leading to strong magnetic interaction.[23] The Au surface of the spiky outer shell additionally enables surface functionalization (through thiol chemistry) and acts as an efficient SERS substrate. Additionally, the formation of a complete gold shell around the iron oxide core prevents oxidation and degradation of IONPs in biological environments, which has been shown in previous studies.[24,25] In this configuration, the magnetic iron oxide core acts as an effective T_2 negative contrast agent, whereas the outer gold shell is functionalized with RaRs for SERS and can be subsequently wrapped with biocompatible polymers, labeled (or not) with fluorescent dyes. The plasmonic (SERS) response of these hybrid NPs, which we herein denote IOAuNS, is defined by the morphology of the spiky gold shell, with tip-localized plasmon modes within the first biological transparency window (NIR-I; 650 − 950 nm), thereby maximizing light penetration depth. We illustrate the multimodal nature of this nanoparticle system through correlative imaging based on the magnetic, plasmonic, and fluorescent properties of IOAuNS, in various biological models (2D cell cultures, 3D spheroid models, and *ex situ* brain tissue), thereby highlighting the challenges involved in the characterization of biological models with varying complexity.

METHODS

Materials

Ferric chloride hexahydrate (FeCl$_3$·6H$_2$O, ≥98% Sigma-Aldrich), poly(vinylpyrrolidone) (PVP360; Sigma-Aldrich), sodium acetate anhydrous (ReagentPlus ≥99.0% Sigma-Aldrich), ethylene glycol (ReagentPlus, ≥99% Sigma-Aldrich), absolute ethanol (CH$_3$CH$_2$OH, Sigma-Aldrich), hydrogen tetrachloroaurate trihydrate (HAuCl$_4$·3H2O, ≥99.9% Sigma-Aldrich), sodium citrate tribasic dihydrate (≥98% Sigma-Aldrich), sodium borohydride (NaBH$_4$, ReagentPlus, 99%, Sigma-Aldrich), silver nitrate (AgNO$_3$, ≥99% Sigma-aldrich), L-ascorbic

acid (AA, ≥99% Sigma-Aldrich), hydrochloric acid solution (HCl 37 wt% Panreac), 2-naphthalenethiol (2-NAT, 99% Sigma-Aldrich), 4-biphenylthiol (4-BPT, 97% Sigma-Aldrich), chloroform (CHCl$_3$, ≥99.8% Sigma-Aldrich), HS-PEG-COOH (MW 3.000 Dalton, Iris Biotech), DY633 (λ_{ex} = 637 nm, λ_{em} = 657 nm, Dyomics,) and TAMRA (Molecular Probes, Life Technologies, #A1318, λ_{ex} = 544 nm, λ_{em} = 571 nm, Fisher scientific) were prepared and used without further treatment. Milli-Q water was used for all the experiments.

NP synthesis methods

Multicore IONP Synthesis: For the preparation of multicore IONPs, a previously reported synthetic procedure was followed.[26] Briefly, 0.21 mmol of iron chloride hexahydrate was dissolved in 36.3 mL of ethylene glycol under stirring. Then, 516.6 μmol of PVP360 was slowly added to the solution under vigorous stirring and the solution was heated (< 100 °C). When the reactants were completely dissolved, 5.2 mmol of sodium acetate was added to the solution. The mixture was placed in a Teflon autoclave and heated in a drying oven for 4 h at 200 °C. Finally, the solution was cooled down and the particles were washed twice by centrifugation (9000 rpm, 20 min) with ethanol and one additional wash with milli-Q water.

AuNP Synthesis (4nm): For the synthesis of 4 nm Au seeds, a previously reported method was used.[27] In brief, 0.6 mL of freshly prepared 0.1 M NaBH$_4$ solution was quickly added under vigorous stirring to a 20 mL of solution containing 2.5×10^{-4} M HAuCl$_4$ and 2.5×10^{-4} M sodium citrate. The formation of Au NPs was immediately observed by a color change. The colloidal dispersion was stored at 4 °C and used as seeds within 2-5 h.

AuNP Synthesis (15nm). For the synthesis of 15 nm Au seeds, 95 mL of 0.5 mM $HAuCl_4$ was mixed under vigorous stirring and heated until boiling and then 5 mL of 34 mM citrate solution was added. After 15 min of boiling, the solution was cooled down and stored at 4 °C.

IOAuNP Synthesis. For the decoration of IONPs with 4 nm AuNPs,[28] 5 mL of iron oxide nanoparticles [Fe] = 14 mM (Z-potential: -2 mV) was placed in a 40 mL glass vial and separated using a magnet, followed by removal of the solution and addition of 25 mL of gold nanospheres at the desired concentration (**Table S1**) (Supporting Information). The mixture was left under sonication for 30 min and stirred in a vortex mixer for 1.5 h. The product was washed several times with the help of a magnet, to ensure complete removal of the gold nanospheres that were not attached to IONPs. The final gold concentration of IOAuNP was analyzed by ICP-MS.

IOAuNS Synthesis. Typically, 10 mL of $HAuCl_4$ at different concentrations were placed in a 20 mL glass vial. Then, HCl was added and immediately after, a solution containing the IOAuNSs was incorporated as seeds, the concentration of gold being varied as shown in **Table S2**. Then, $AgNO_3$ and ascorbic acid were simultaneously and quickly added to the solution. A fast change from brown to blue indicates gold nanostar formation. Subsequently, HS-PEG-COOH was added to stabilize the final particles. The different amounts and concentrations of the reactants used for the fabrication of IOAuNSs are summarized in **Table S2**. The solution was stored at 4 ºC until further use. Due to the magnetic nature of the IOAuNSs, for all the reactions a specially designed stirrer made of polylactic acid (PLA) was 3D-printed and connected to a mechanical stirrer to ensure effective mixing of the reactants (**Figure S1**).

SERS encoding of IOAuNSs. The probes were encoded using different Raman-active molecules, following an established protocol based on successive phase transfer.[10] Briefly, 5 mL of

IOAuNPs (total concentration of metals [Au+Fe]=1.5 mM]) was placed in a test tube. 2 mL of 4-BPT 10 mM in chloroform and 16 μL of HCl were added and the mixture was stirred for 2 h to enable phase transfer. Finally, the particles located in the organic phase (bottom phase) were recovered and washed twice with chloroform by centrifugation (9000 rpm, 5 min).

PMA functionalization of IOAuNSs. The dispersion of IOAuNS@4-BPT or IOAuNS@2-NAT was placed in a round-bottom flask and 100 μL 0.05M of dodecylamine-modified polyisobutylene-alt-maleic anhydride amphiphilic polymer (PMA) was added and stirred. The solvent was evaporated in a rotary evaporator and the particles redispersed in 5 mL of water and 1 mL of NaOH pH = 12. The particles were washed three-fold by centrifugation (9000 rpm, 5 min) or until neutralization. The PMA used to wrap the Raman-encoded IOAuNS was prepared following previous reports.[10,29] PMA comprises polyisobutylene-alt-maleic anhydride (hydrophilic backbone) on which 75% of the anhydride rings have been reacted with dodecylamine (hydrophobic chain). The polymer structure is represented in **Figure S2.**

PMA functionalization with fluorescent dyes. Labeling of NPs with fluorophores was performed on PMA functionalized with TAMRA dye and DY633 dye (see **Figure S3**). The procedure was conducted as previously reported.[30] The excitation and emission spectra of the particles coated with the dye- modified polymer are shown in **Figure S4**.

NP characterization

Standard characterization. All NPs were characterized using TEM, ICP-MS, and UV-Vis-NIR. UV−vis-NIR extinction spectra were recorded using an Agilent 8453 UV−Vis diode array spectrophotometer, normalizing spectra at 400 nm. ICP-MS analysis was conducted using an ICP-MS Agilent 7500ce to determine the concentration of Au and Fe. Samples containing

biological material (cells or spheroids) were digested in *aqua regia* during 48 h, followed by addition of H_2O_2 and continued heating until a clear and transparent solution was observed. The samples were cooled down to RT and subsequently measured. TEM images were collected with a JEOL JEM-1400PLUS transmission electron microscope operating at 120 kV, using carbon-coated 400 square mesh Cu grids.

Z-Sizer measurements. A Malvern Zetasizer 3000 HS particle size analyzer (Malvern Instruments, UK) was used to measure zeta-potential and dynamic light scattering (DLS), from which hydrodynamic diameter distributions were obtained. Samples were placed in disposable cuvettes of 1 cm optical path length using a diluted (1:100) NP solution, using distilled water as solvent. The width of the DLS hydrodynamic diameter distribution is characterized by the polydispersity index (PdI). In the case of a monomodal distribution (Gaussian) calculated by means of cumulant analysis, $PdI = (\sigma/Z_{avg})^2$, where σ is the width of the distribution and Z_{avg} the average diameter of the particle's population, respectively.

Electron Tomography. IOAuNSs were diluted in H_2O to a final concentration of 0.05 mM, and drop-cast on a carbon-coated 400 square mesh Cu grid. The samples were then left to dry at ambient temperature. TEM images were acquired using an aberration-corrected 'cubed' Thermo Fisher Scientific-Titan electron microscope operated at an acceleration voltage of 300 kV, with a camera length of 58 - 105 mm. Atomic resolution scanning TEM (STEM) high angular annular dark field (HAADF) images were acquired using a convergence angle of 20 mrad. Tomography tilt series were acquired using a Fischione 2020 tomography holder over $\pm$ 76 ° with tilt increments of 2 º. Typically, each angle consisted of a 1k x 1k STEM HAADF image using 12 ms dwell time. The images acquired manually at each angle were aligned with respect to each other and the tomograms rotation axis was determined with mathematical precision through

phase correlation. Finally, the 3D reconstruction was achieved using 25 SIRT cycles. A bandwidth limit was also applied to the SIRT reconstruction in real and Fourier space to achieve a high-quality reconstruction with minimized missing wedge artefacts.

STEM EELS Imaging. Fe oxidation state was determined by electron energy loss spectroscopy (EELS) using an aberration-corrected 'cubed' FEI-Titan electron microscope operated at an acceleration voltage of 200 kV. Lower acceleration voltages were tried, however this led to significant cupping artefacts. The energy resolution provided by the electron monochromator, as measured from the full-width at half maximum of acquired zero-loss peaks was 0.2 eV, the dispersion of the spectrometer was set to 0.01 eV/ch and 2,000 channels are used to cover an energy range from 704 eV to 724 eV, being the entire Fe L2,3 edge. The pixel size equals 1.8 nm (65x65 pixels) for higher magnification single-particle EELS mapping, which is sufficient to distinguish any variation in oxidation state throughout the nanoflower's sub-structure. Lower magnification EELS maps with a pixel size of 20 nm^2 was used to determine oxidation state variation within different nanoflowers from both samples.

Surface Area Measurement. To extract the accessible and external Au surface area relevant for further functionalization, Fe and Au phases were identified by a manual segmentation process using Amira software. As the Au surface contained voids and areas of exposed Fe_2O_3 core, the total Fe surface could not be directly subtracted from the total surface (internal and external Au surface) of Au. Rather, the Fe surface in contact with Au must be calculated first, so that accurate accessible Au surface areas could be derived. Using a surface generation module, boundary surfaces can be extracted and later removed for a final Au surface area.

SERS. Characterization of the SERS signal of IOAuNS@4-BPT and IOAuNS@2-NAT was performed with a Raman microscope (inVia Reflex, Renishaw, Wotton-under-Edge, U.K.) equipped with a −60 °C Peltier-cooled front-illuminated CCD detector (1024 × 512 pixel^2 chip), using a 785 nm laser excitation source (maximum output 270 mW) and a 1200 lines/mm diffraction grating. For the experiments 300 µL of each aqueous solutions was placed in a glass vial. SERS spectra were collected using a 10× objective (NA = 0.25; Leica Microsystems, Wetzlar, Germany) in expanded scan mode, with an integration time of 10 s and at a laser power of 52.5 mW. All the spectra were analyzed using the WiRE4.4 software (Renishaw, Wotton-under Edge, U.K.) to eliminate cosmic rays and the correction of the baseline in the spectra was performed on Matlab, using the Beads function.

Magnetism. ZFC/FC measurements were performed at 100 Oe and within a temperature range of 5-300 K, using a Quantum Design MPMS3 VSM-SQUID magnetometer with a sensitivity of 10^{-8} emu up to a maximum field of 7 T. The hysteresis loops were measured in a Vibrating Sample Magnetometer (VSM) with a sensitivity of $5 \cdot 10^{-6}$ emu, up to a maximum field of 18 kOe working at room temperature.

Cell culture

MCF7 cells were purchased from the ATCC. Human Dermal Fibroblasts (HDF), fetal bovine serum (FBS), penicillin-streptomycin (PS), DMEM, lactate dehydrogenase (LDH) assay, and NucBlue were purchased from Invitrogen. Propidium iodide (PI) was purchased from Sigma. MCF7 and HDF cells were grown in DMEM supplemented with 10% FBS and 1% PS (herein termed complete DMEM, cDMEM).

IOAuNS cytotoxicity tests. The cytotoxicity of IOAuNSs in MCF7 cells was evaluated using the LDH assay and PI staining. Cells were seeded at 1.6 x 10^5 cells/cm^2 in 96-well plates to analyze the cytotoxicity by LDH assay, and at 9 x 10^4 cells/cm^2 in 96-well imaging plates (Ibidi) for characterization by microscopy. The following day, IOAuNS were added at concentrations ranging from 0.25 mM to 0.031 mM (total metal ion concentration). After 24 h, the NP solution was removed and rinsed with media. The media was renewed again 6 h later to remove IOAuNSs in suspension and on the bottom of the plate. The presence of aggregated NPs was monitored daily by optical microscopy. The LDH test was performed using the standard protocol 48 h post addition of IOAuNSs. For analysis via imaging, PI was added to a final concentration of 500 nM, and nuclei stained using NucBlue. Images of 1 x 1.3 mm^2 were acquired with a Cell Observer microscope (Axio Observer, Zeiss) 48 h after the addition of IOAuNSs. Post-processing and quantification of cells were conducted with ImageJ, and data represented as a percentage of dead cells.

Spheroids formation. Spheroids were formed from cells, with and without pre-incubation steps with IOAuNSs. In the case of spheroids which were exposed to IOAuNS post formation, MCF7 and HDF cells were mixed in a 1:1 ratio using a final cell number of 1.7x10^4 cells/spheroid (μ-shaped plate growth method) and left for 3 days to form the spheroid. A 25 μL dispersion of IOAuNSs (1:1 mix of IOAuNS@4-BPT@TAMRA and IOAuNS@2-NAT@DY633, final ion concentration 0.05 mM) in cDMEM was made in a 500 μL eppendorf and ca. 5 spheroids added. Using a rotisserie rotator placed in an incubator at 37 °C, 5% CO_2, spheroids were rotated during 24 h to help achieve an even distribution of IOAuNSs around spheroids. Spheroids were subsequently retrieved and used for imaging studies or fixed using 4% formaldehyde for later imaging and embedding in OCT freezing media.

For spheroids exposed to IOAuNSs pre-formation, MCF7 and HDF cells were seeded in 12-well plates (8 x 10^4 MCF and 6 x 10^4 HDF cells/mL) and once adhered, IOAuNS@4-BPT@TAMRA and IOAuNS@2-NAT@DY633 were added to MCF7 and HDF cells, respectively, at a final concentration of 0.05 mM. After 24h, non-endocytosed IOAuNSs were removed via washing, and cells detached using trypsin-EDTA. Cells were readjusted to 8.6 x 10^4 cells/mL and mixed in a 1:1 ratio. Cells (1.7x10^4 cells, 200 μL) were added to μ-shaped 96-well plates and incubated at 37 °C, 5% CO_2 for 3 days for spheroid formation to occur. Spheroids were subsequently retrieved and used for imaging studies or fixed using 4% formaldehyde for later imaging and embedding in OCT freezing media.

Multimodal imaging

Cell preparation: 2D SERS mapping was conducted using MCF7 cells preincubated with IOAuNSs from series a, b and c. In brief, MCF7 cells were seeded at 2.8 x 10^4 cells/cm^2 in 12-well plates and allowed to adhere. The following day, IOAuNSs diluted in cDMEM were added (0.05 mM final total ion concentration) and after 24 h, non-endocytosed IOAuNSs were removed and cells detached using trypsin-EDTA. For SERS imaging, cells were seeded in 35 mm glass-bottomed dishes (5 x 10^4 cells/dish) and after 2-3 h of incubation, SERS mapping undertaken using the settings described below. For MRI, a volume containing 2 x 10^5 cells was centrifuged and resuspended to 400 μL of PBS. Subsequently, 100 μL (containing 5 x 10^4 cells) was dispersed into each well of the phantom for MRI imaging. For ICP measurements, a volume of cell solution containing 5 x 10^4 cells was centrifuged, concentrated in 50 μL PBS, and frozen at -20 ºC. To promote cell lysis, three freeze-thaw cycles were performed. The samples were subsequently digested using aqua regia, aided by microwave digestion (**Table S3**). For fluorescence confocal imaging, 1.3 x 10^4 cells (1:1 mix of HDF and MCF7 cells previously

exposed to IOAuNS@4-BPT@TAMRA and IOAuNS@2-NAT@DY633, respectively) were seeded in 35 mm glass-bottomed dishes with a 500 μm etched grid (Ibidi) and allowed to adhere. The following day the media was removed, and samples fixed and permeabilized using 4% formaldehyde and TritonX-100. Immunostaining to identify MCF7 and HDF cells was carried out using antibodies against E-cadherin and TE7 (both Novusbio), respectively. Appropriate matching secondary antibodies with AlexaFluor 405 and 633 fluorescent labels were used at a 1/400 dilution. Samples were stored in PBS at 4 °C until imaged.

SERS imaging of cells. SERS measurements were performed with a Raman microscope (inVia Reflex, Renishaw, Wotton-under-Edge, U.K.) equipped with a -60 °C Peltier-cooled front-illuminated CCD detector (1024×512 pixel^2), using a 785 nm laser excitation source (maximum output 270 mW) and a 1200 lines/mm diffraction grating. SERS maps were recorded in static mode (centered of scattered wavenumber 1450 cm^{-1}) using a 40× dip-in water immersion objective (numerical aperture, NA = 0.8; Nikon Corporation, Tokyo, Japan). For single cell measurements, areas of ca. 30×30 μm^2 containing one single cell, were imaged with 0.5 s integration time, at 12.08 mW laser power at the surface and a step size of 2 μm. All the spectra were first analyzed using the WiRE 4.4 software (Renishaw, Wotton-under Edge, U.K.) to correct the baseline in the spectra (intelligent 11th polynomial order) and eliminate cosmic rays. Then, the maps were analyzed with a MLRA-based supervised algorithm developed in a previous work,[32] to represent in the cellular images only the spectra similar to the SERS signal of the corresponding nanoparticles.

SERS imaging of spheroids. SERS mapping of spheroids involved placing individual spheroids inside a home-made holder,[31] on top of a small drop of dental glue to fix the spheroid position.

SERS mapping along xz was performed in a Renishaw Raman microscope (inVia Reflex, Renishaw, Wotton-under-Edge, U.K.). An area of 800 × 430 μm^2 was imaged with 0.7 s integration time, 12.08 mW laser power at the surface and a step size of 6 μm and 10 μm in *x* and *z* directions, respectively.

Additional SERS measurements of the spheroids were performed with a WITec confocal Raman microscope (Alpha300R, WITec GmbH, Ulm, Germany) equipped with a −60 °C Peltier-cooled CCD detector (1024 × 128 pixel^2 chip), using a 785 nm laser excitation source (maximum output 83 mW) and a 300 lines/mm diffraction grating. The center of scattered wavenumber was set to 1450 cm^{-1}, and the signal was recorded using a N-achroplan 20× dip-in water immersion objective (NA = 0.5; Zeiss, Jena, Germany). For the measurement of the outer edge of a live spheroid, a volume of 84 × 84 × 70 μm^3 was imaged with a 5 mW laser power, 0.01 s integration time, and step size of 2 μm in xy and 5 μm in z directions. For the transversal cut, an area of 360 × 560 μm^2 was imaged with a 10 mW laser power, 0.1 s integration time, and step size of 5 μm. For post-incubated spheroids a volume of 400 × 380 × 150 μm^3 containing a quarter of the spheroid, was imaged with a 10 mW laser power, 0.1 s integration time, and step size of 5 μm in *xy* and 10 μm in *z*. For the measurement of the spheroid slice, an area of 635 × 875 μm^2 was imaged with a 10 mW laser power, 0.1 s integration time, and step size of 5 μm. Prior to data analysis, SERS spectra were pretreated by cosmic ray removal and background subtraction (Shape 100), both implemented in the Project FIVE plus software (WITec, Um, Germany). To identify the known Raman reporter spectrum, the TrueComponent tool, also embedded in the same software package, was applied.

Ex-vivo sample preparation. A mouse brain was extracted from a cadaveric specimen provided by our animal facility (no animals were expressly used for this study) and casted in a falcon tube

with 15mL of agarose solution (1.6% w/v). Then, 5 μL of IOAuNS@2-NAT@DY633, cells incubated with IOAuNS@2-NAT@DY633 and PBS were injected in the tissue with the help of a stereotaxic frame and a Hamilton syringe. After MRI imaging studies, the brain was extracted from the agarose, and then it was immersed in formalin 10% overnight and posteriorly in sucrose (30%) in PBS solution for two days, for fixation and cryopreservation of the tissue. Finally, the brain was frozen and kept at -80°C until posterior use.

SERS imaging of brain slices. SERS imaging of brain histology slices was carried out on top of a quartz slide. SERS measurements were performed with a confocal Raman microscope (Alpha300R, WITec GmbH, Ulm, Germany) equipped with a −60 °C Peltier-cooled CCD detector (1024 × 128 pixel^2 chip), using a 785 nm laser excitation source (maximum output 83 mW) and a 300 lines/mm diffraction grating. The center of scattered wavenumber was set to 1450 cm^{-1}, and the signal was recorded using a 20× objective (NA = 0.4; Nikon Corporation, Tokyo, Japan). For SERS measurements of brain samples, two areas of 680 × 250 μm^2 and 350 × 350 μm^2 were imaged with a 5 mW laser power, 0.05 s integration time, and step size of 3 μm. Prior to data analysis, SERS spectra were pretreated by cosmic ray removal and background subtraction (Shape 100), both implemented in the Project FIVE plus software (WITec, Um, Germany). To identify the known Raman reporter spectrum, the TrueComponent tool, also embedded in the same software package, was applied.

Confocal fluorescence microscopy. Fluorescence images of biological samples were obtained with a Zeiss 880 confocal microscope. To image whole spheroids, the sample was immobilized in a 0.5 cm silicon well printed on a coverslip (total volume ca. 50 μL), with a 1 cm circular glass cover slip placed on top to avoid evaporation. TAMRA- and Dy633-containing IOAuNSs were imaged using 561 and 633 nm laser sources, with detectors set to ca. 595 ± 25 nm and 680 ± 25

nm, respectively. A Plan-apochromat x10 objective (NA = 0.45, Zeiss) was used to obtain z-stacks of ca. 200 μm. A 3-pixel mean filter was applied prior to obtaining Maximum Intensity Projections (MIP). 2D images of co-cultured HDF and MCF7 cells, pre-incubated with IOAuNS@4-BPT@TAMRA and IOAuNS@2-NAT@DY633, respectively, were also obtained using a Plan-apochromat x20 objective (NA = 0.8, Zeiss) and 405, 488, 561, and 633 laser excitation sources. For brain imaging, slices were cut using a cryotome and collected on quartz slides. A Plan-apochromat x10 objective (NA = 0.45, Zeiss) was used with 633 nm excitation. The tile-feature of the ZEN software what used to produce an overview of the whole brain slice.

MRI Phantom imaging. Agar was solved in hot water (15 mL, 1.6% w/v), placed in a plastic mold and left to solidify at room temperature. Once hardened, 32 wells of 2 mm of diameter were drilled in the gel. To have a perfectly flat bottom in each well, 20 μL of 0.4% agar solution was pipetted into the base of each well and left to solidify. Then, 50 μL of the desired sample was deposited in each well and completely covered with 0.9% agar solution. A scheme of the phantoms containing the distribution of the holes and the concentrations of the samples is shown for cells in **Figure S5A** and for spheroids in **Figure S5B.**

MRI imaging of brain slices. The brain images were performed in a 11.7 T horizontal bore Bruker Biospec 117/16 USR scanner (Bruker Biospin, Ettlingen, Germany).

Biological TEM. Cells and spheroids were prepared for TEM imaging by first fixing the sample with 2% formaldehyde / 2.5% glutaraldehyde in Sorensen's buffer, followed by OsO_4 fixation/staining and dehydration in an ethanol series. Finally, samples were embedded in Spurr´s resin, followed by cutting 100 nm thick slices using an ultramicrotome.

RESULTS AND DISCUSSION

Synthesis of magnetic-plasmonic nanoparticles

Multicore iron oxide nanoparticles (IONPs) were prepared by means of a polyol-mediated solvothermal synthesis approach,[26] with slight modifications. Briefly, iron (III) chloride was dissolved in ethylene glycol, a short-chain polyol, followed by addition of poly(vinylpyrrolidone) (PVP; MW 360 kD) as a capping agent. Next, sodium acetate (NaAc) was incorporated to the reaction mixture to promote the hydrolysis of Fe^{3+} ions, thereby controlling both nucleation and the final particle morphology. As can be observed in **Figure S6A**, this process results in the formation of maghemite (γ-Fe_2O_3) IONPs, composed of multiple 5 nm crystallites adding up to a final average diameter of 119 ± 25 nm, as measured by transmission electron microscopy (TEM). From prior literature, we expect the synthesized IONPs to provide our system with the appropriate magnetic properties for use as T2 contrast agents.[32]

The coating of IONPs with a spiky Au shell comprised two synthetic steps. IONPs were first decorated by addition of pre-made Au NP seeds, which spontaneously adsorb on the IONP surface and subsequently act as nucleation points for growth and branching into the final Au shell. A scheme of the synthetic process of each step is shown in **Figure 1A**. We investigated the use of AuNPs with diameters of 4 nm and 15 nm as seeds (**Figure S6B**), synthesized using previously described methods.[27,33] Whereas uniform surface adsorption was observed for both NP types (**Figure S6C**), a higher density of adsorbed NPs was achieved using 4 nm AuNPs, leading to a better control over shell growth. We thus proceeded with this sample, to optimize the density of AuNPs on the IONP surface, for subsequent spike growth. By increasing the relative concentration of AuNPs with respect to that of IONPs, surface coverage was gradually increased

(**Figure S7**). However, conventional 2D TEM imaging is insufficient to accurately determine the density of AuNPs at the IONPs surface and therefore, electron tomography was applied (**Figure S8A,B**). In the final step, the growth of sharp tips was promoted by seeded growth on the iron oxide-supported Au seeds, by adapting a reported procedure for surfactant-free AuNS.[30] Electron tomography was used to reveal the 3D configuration of the shell and the sharp tips therein (**Figure S8C).** The branching degree of the resulting IOAuNSs could be finely tuned by gradually varying the amount of $HAuCl_4$ added in the final growth step (**Figure 1, Figure S9**). To summarize, IOAuNSs with smaller overall diameters were obtained from iron oxide cores with a lower density of AuNPs (series a-c in **Figure 1B**). Additionally, longer spikes and hence overall larger IOAuNSs were grown when increasing the amount of $HAuCl_4$ added in the growth step (sequence I-IV in **Figure 1B).** The inorganic core-shell size of IOAuNS was carefully evaluated from TEM images (**Table S4, Figure S10)**.
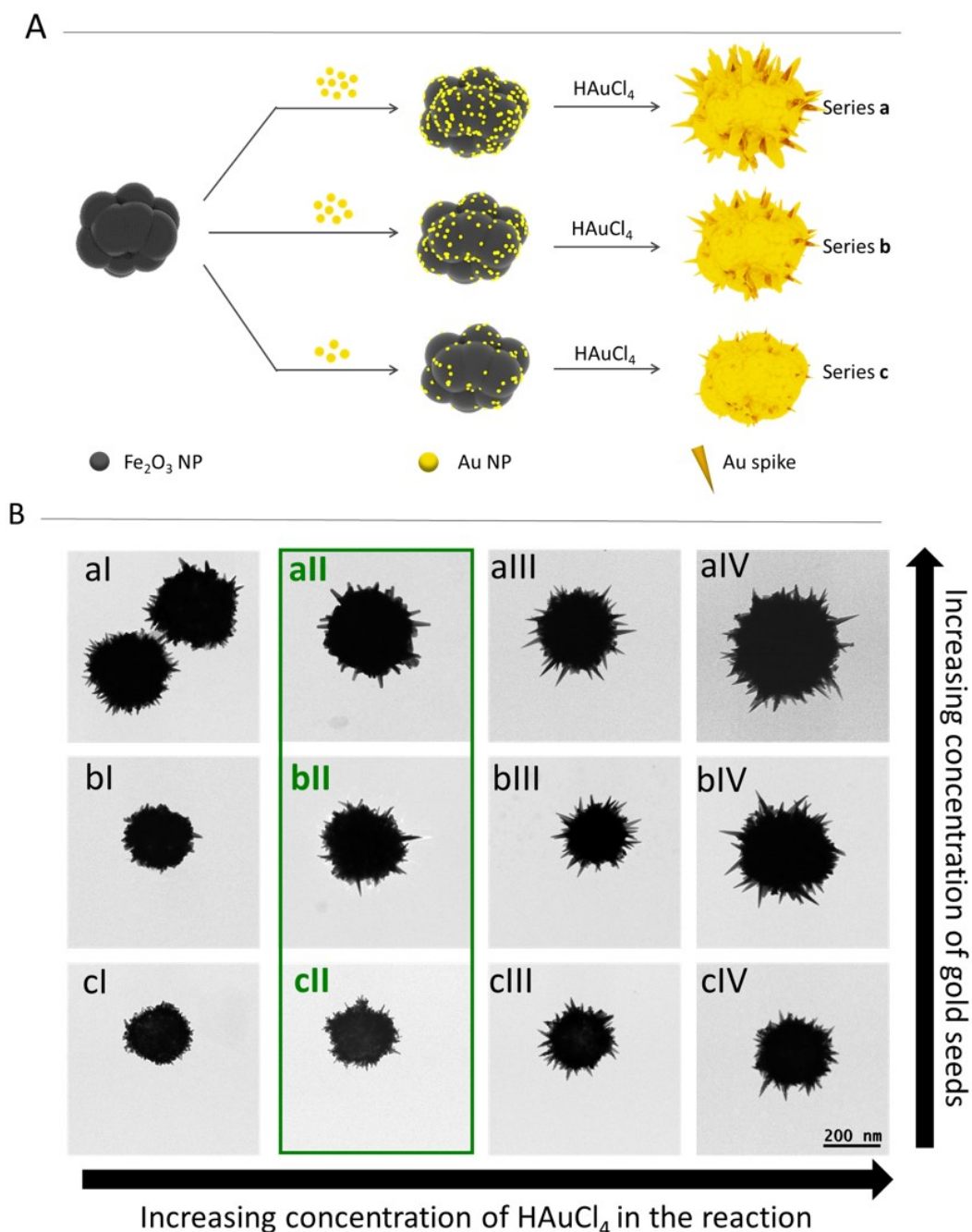
Figure 1. (A) Scheme of the various steps involved in the synthesis of IOAuNS, comprising the addition of varying amounts of AuNPs onto IONPs and subsequent reduction of $HAuCl_4$ to obtain different spiky shell structures. **(B)** TEM images of IOAuNS obtained from series a-c (increasing AuNP coverage), and I-IV (increasing added $HAuCl_4$). Series II (highlighted in a green box) was selected for further experiments. All the images are at the same magnification. Additional low magnification TEM images are provided in **Figure S9**. The [Au]/[Fe] molar ratios, measured by ICP-MS, are: aI=3.6, aII=2.7, aIII=2.6, aIV=0.97, bI=1.7, bII=1.2, bIII=1.0, bIV=0.2, cI=0.58, cII=0.35, cIII=0.25, cIV=0.13.

Electron microscopy analysis

To obtain quantitative information about the thickness and structure of gold shells (e.g., number of spikes) covering the iron oxide cores, a detailed characterization by electron microscopy and electron tomography was carried out. Such an analysis is important to evaluate the surface area for each IOAuNS sample, which is in turn needed toward optimization of further coating and functionalization steps. For all experiments, IOAuNS series II was chosen because it yields smaller IOAuNS, while maintaining the presence of well-defined spikes (**Table S4**). Additionally, electron tomography experiments are facilitated by minimizing artifacts that may appear at relatively large thickness. As shown in **Figure 1B**, for a fixed amount of added HAuCl4, thicker gold shells are obtained when increasing the initial coverage of IONP cores with AuNPs. Representative 3D visualizations of the structures retrieved by high-angle annular dark field (HAADF) electron tomography are shown in **Figure 2**. Our results showed complete gold shell formation for samples aII and bII, but defects were observed for cII **(Figure 2A)**. Careful inspection of orthoslices through 3D reconstructed data sets yielded the average gold shell thickness for samples aII (75 ± 15 nm), bII (66 ± 12 nm) and cII (24 ± 5 nm), as illustrated in **Figure 2B**.

Electron tomography results additionally provide reliable values of the IOAuNS surface area, which are required for further surface functionalization. Using a manual segmentation process and a surface generation module, boundary surfaces were extracted for Au surface area determination (see details in Methods and surface area values in **Figure S11**). Interestingly, the experimental values were in agreement with a geometrical model, based on a hexagonal arrangement of spikes with randomly assigned lengths (see more details on the model in the SI).
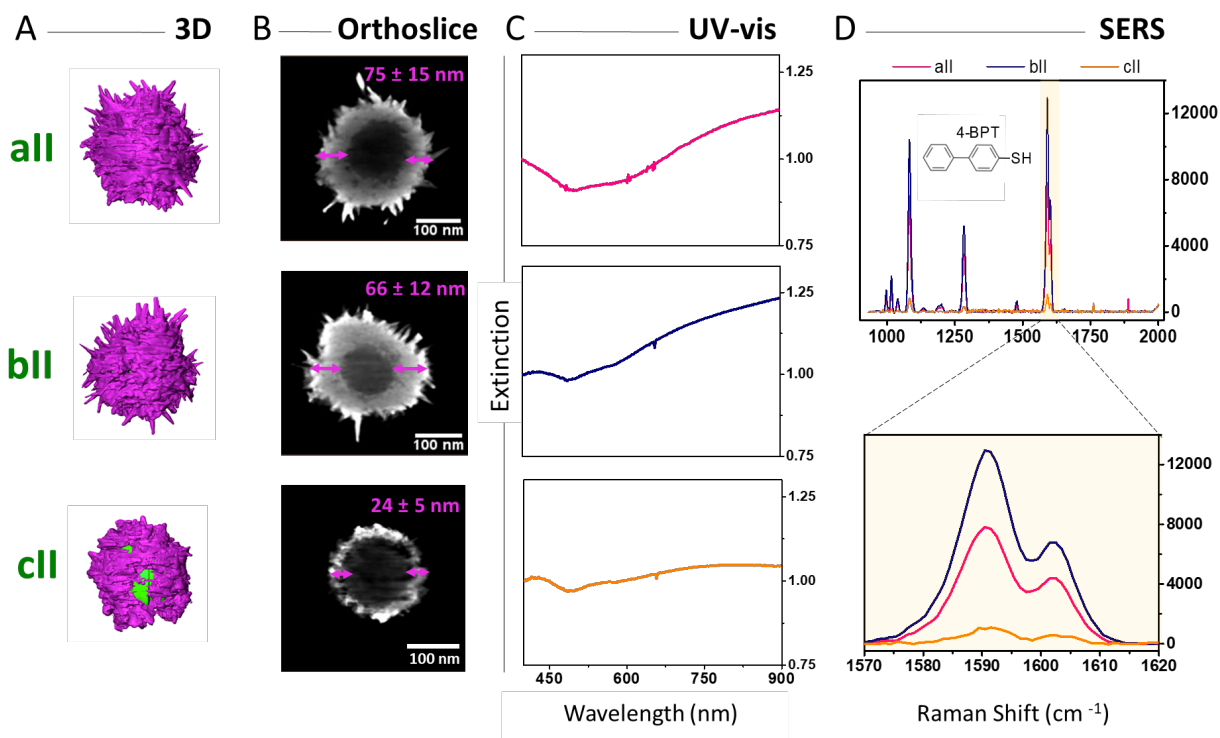
Figure 2. (A) Representative 3D visualizations of electron tomography reconstructions corresponding to particles aII, bII and cII. **(B)** Orthoslices through the 3D electron tomography reconstructions shown in (A). The double-head arrows indicate the thickness of the gold shells. **(C)** Normalized (@400 nm) UV-vis-NIR spectra for the different samples in IOAuNS@4-BPT series II. **(D)** SERS spectra from IOAuNS@4-BPT series II. Spectra were measured in aqueous dispersion, at the same iron concentration, [Fe] = 0.1 mM.

Magnetic properties

We recorded zero-field cooled (ZFC) and field cooled (FC) magnetization curves, as well as magnetic hysteresis loops, to characterize the magnetic response from the iron oxide cores.[34] The Fe_2O_3 composition of the cores was first confirmed by electron energy loss spectroscopy (EELS), using IOAuNS bII as a representative sample (**Figure S12A,B**). To test for potential further oxidation over time, which would affect the magnetic properties, hysteresis loops were recorded for both freshly prepared and aged (6 months post-synthesis) IONPs. A saturation magnetization of 50 Am^2/kg was measured in both cases (**Figure S12C**), which is slightly lower

than the saturation magnetization of bulk maghemite (74 Am^2/kg),[35] likely due to surface disorder effects on Fe_2O_3 nanoflowers.[36] Additionally, comparison of ZFC/FC curves for IONP and IOAuNSs indicated no significant changes in the magnetic properties at constant magnetic field (**Figure S12D**), suggesting that the presence of the Au shell has not effect on the magnetic properties of the iron oxide cores, in agreement with previous reports.[12] Taken together, these results confirm a maghemite phase of IONPs with only negligible traces of the Verwey transition[37] and a near-superparamagnetic behavior characterized by low remanence and coercivity.

SERS encoding

It is well-known that AuNPs can be readily functionalized with thiolated molecules, due to the stability of thiol-metal bonding. We therefore selected two standard thiolated Raman-active reporter molecules, namely 4-biphenylthiol (4-BPT) and 2-naphthalenethiol (2-NAT), for surface functionalization and encoding of IOAuNS, required for subsequent SERS imaging. RaR adsorption onto IOAuNSs was promoted by using a previously reported phase-transfer method,[38] in which the nanoparticles are transferred into an organic solvent containing the Raman reporter, and subsequently coated with PMA, thereby resulting in the SERS-encoded IOAuNS versions: IOAuNS@4-BPT and IOAuNS@2-NAT. The addition of an external PMA layer renders IOAuNSs hydrophilic, thus allowing their redispersion in water for further use in biological environments. Raman shifts for the most prominent vibrations in 4-BPT and 2-NAT are listed in **Table S5**. A complete analysis of the average hydrodynamic diameter of the encoded IOAuNSs is shown in **Table S4** and **Figure S10**.

All IOAuNS samples were successfully encoded with Raman reporter molecules; UV-vis-NIR and SERS spectra for the complete series (a-c and I − IV), are shown in **Figure S13**. Taking into account morphology considerations (see above), IOAuNS@4-BPT series II were studied in detail. SERS measurements were performed by fixing the NP concentrations, based on iron content ([Fe] = 0.1 mM), as opposed to gold, so that we could study the role of the gold shell thickness and morphology on SERS intensity. Considering that biological tissues are particularly transparent at wavelengths between 650 and 950 nm (first biological window, BW-I) and that IOAuNS were selected to display LSPR within the NIR range, a 785 nm laser was used for all SERS measurements. All of the studied IOAuNSs display a significant absorbance within the BW-I, as shown in **Figure 2C**. At the excitation laser wavelength of 785 nm, a higher SERS intensity was recorded for 4-BPT in IOAuNS bII (**Figure 2D**). It has been widely reported that the presence of well-defined spikes within the structure of Au NPs can strongly contribute to the enhancement of the Raman signal of adsorbed molecules, acting as intrinsic hotspots. In this regard, the significantly lower SERS intensity recorded for particles cII is likely due to the less defined and more polydisperse spikes, as reflected by a broader LSPR band.[39]

Multimodal cell imaging

The use of nanoparticles as contrast agents in any biological application requires biocompatibility, stability and, in most cases, efficient cellular uptake. We verified the uptake of IOAuNS by conducting SERS mapping of MCF7 cells after incubation with IOAuNS@4-BPT. The results are summarized in **Figures 3A** and **S14**, confirming the co-localization of IOAuNS with MCF7 cells. Additional high resolution 3D SERS maps of MCF7 cells incubated with IOAuNS@4-BPT-bII were also conducted to better determine their spatial distribution within a

single cell (**Figure S15**). As the 2D image and the 3D reconstruction from confocal Raman microscopy indicate, IOAuNS@4-BPT seem to be organized inside vesicles, suggestive of endosomes, throughout the volume of the cell. Similar conclusions could be made from TEM imaging of resin-embedded MCF7 cells (**Figures 3B** and **S16**). Importantly, no sign of cytotoxicity was observed, which was confirmed by exposing MCF7 cells to different concentrations of IOAuNS@4-BPT-bII for 24 h, followed by cytotoxicity analysis using the commercial lactate dehydrogenase (LDH assay) and membrane permeability staining (**Figure S17**). These results suggest successful cellular uptake and confirm the biocompatible nature of IOAuNS, which are thus suitable contrast agents for SERS imaging. Additionally, NPs coated with PMA have been proven to be compatible with a wide variety of cell lines.[10]

We proceeded next to analyze the use of the same hybrid NPs as T2 contrast agents for MRI. As the iron oxide core size plays a major role in these experiments, IOAuNS concentrations were adjusted based on the total (Fe + Au) metal concentration. Compared to SERS imaging, a lower IOAuNS concentration was chosen (0.05 mM) because of the increased sensitivity of the technique at these settings. Phantoms were prepared by using an agarose block (40 mm diameter), in which holes (2 mm diameter) were carefully drilled, wherein cells pre-incubated with IOAuNSs were subsequently placed. Each agarose phantom contained a sufficient number of holes to accommodate also appropriate controls, including cell media, water, IONP, and IOAuNS. As can be observed in **Figure 3C**, dark contrast (typical for T2 contrast agents) appeared only in those samples containing IONP and IOAuNS, with or without cells. As expected, higher concentrations of Fe in IOAuNS (c > b > a) resulted in higher contrast (see also **Figure S18**). It should however be considered that, differences in contrast may also be related to thinner or incomplete gold shells, as observed along the various series (see **Figure 2B**), which

may allow water to come into closer contact with the iron oxide core.[40] More concentrated and darker contrast was observed in the MRI images of MCF7 cells with internalized IOAuNSs, most likely due to NP aggregation within endosomes.[41,42] MRI images of the respective samples from the IOAuNS series I-IV are shown in **Figure S18.**
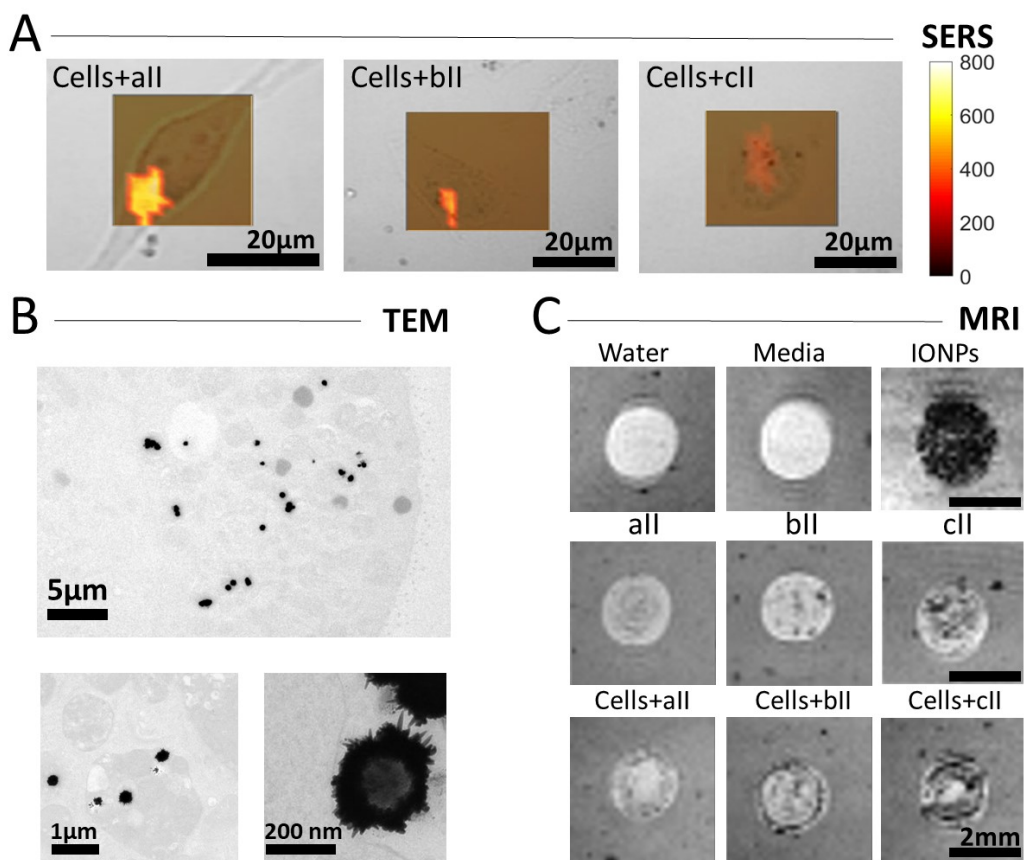
Figure 3. (A) Bright Field TEM images, with overlaid SERS maps, of MCF7 cells pre-loaded with IOAuNS@4-BPT from series II. (B) Representative TEM images of IOAuNS@4-BPT bII internalized inside cells. Additional images are provided in **Figures S12 and S13**. **(C)** MRI images of agarose phantoms containing series II IOAuNS, both alone and incubated with cells, as labeled.

Multimodal imaging in cell spheroids

We next tested the activity of IOAuNS as contrast agents for multimodal imaging in a 3D spheroid cell model. Spheroids constitute an excellent and accessible alternative model to more traditional 2D cell culture studies, as they better represent the complex 3D environment occurring *in vivo*, often incorporating mixed cell types and gradients in nutrients and waste products.[43] Furthermore, the complications involved in NP delivery due to the presence of an extracellular matrix (ECM) or poor NP penetration are better mimicked in spheroids compared to 2D cell experiments.[44] We thus explored the use of spheroids comprising MCF7 cancer cells and fibroblasts (HDF), as a 3D model for multimodal imaging with IOAuNS. We initially pre-labeled the separate cell populations with two different RaR-labeled IOAuNS (from here on, we used IOAuNS-bII for further characterization), which were also fluorescently labeled to allow correlative confocal fluorescence microscopy. To do so, the PMA used to encapsulate IOAuNSs was chemically modified with TAMRA and DY633 fluorescent dyes (see structures in **Figure S3** and optical characterization in **Figure S4**). 4-BPT and 2-NAT were used as Raman reporters, no significant changes in the intensity and the fingerprint of their SERS spectra were detected in the presence of the fluorescent dyes (**Figure S19**).

We selected 4-BPT and 2-NAT because they offer clearly distinguishable fingerprints and can be analyzed using multivariate methods (see **Table S5** and Methods section for details) to differentiate more precisely cell populations in a co-culture system. Thus, MCF7 cells were labeled with IOAuNS@4-BPT@TAMRA, and HDF cells with IOAuNS@2-NAT@DY633 (**Figure S20**). Spheroids were formed using round-bottomed wells, using an initial seeding concentration of 1.7×10^4 cells/spheroid (total combined cells, mixed at a 1:1 ratio; se scheme in **Figure 4A**). Live SERS imaging of the whole spheroid was first carried out to probe the overall location of the multimodal NPs. As shown in **Figure 4B,C**, whereas both RaRs can be clearly

identified in the SERS maps, and 3D reconstructions can be obtained, IOAuNSs appear to be located only at the outer layer of the spheroid. Considering that spheroid-containing cells were pre-labeled with IOAuNSs, this result was unexpected – IOAuNSs should have been distributed throughout the entire spheroid volume. We thus examined a slice of the spheroid after fixation and microtome cutting, by conducting SERS mapping and fluorescence confocal imaging on the central part of the spheroid. As can be observed in **Figure 4D,E**, this measurement confirmed the presence of both types of SERS-encoded NPs throughout the *xy* plane, suggesting that the lack of SERS signal in the center of the spheroid in live samples stemmed from limitations in the penetration depth of the incident laser, loss of laser focus, and backscattered signal to the spectrometer, principally due to the large amount of IOAuNS in the sample, which cause absorption and diffuse multiple scattering of light. We subsequently examined the spheroids using MRI, by placing 5 spheroids per hole in the agarose phantoms. Contrast was clearly observed for the spheroids containing IOAuNS, with intense dark areas corresponding to the spheroids (**Figure 4F).**
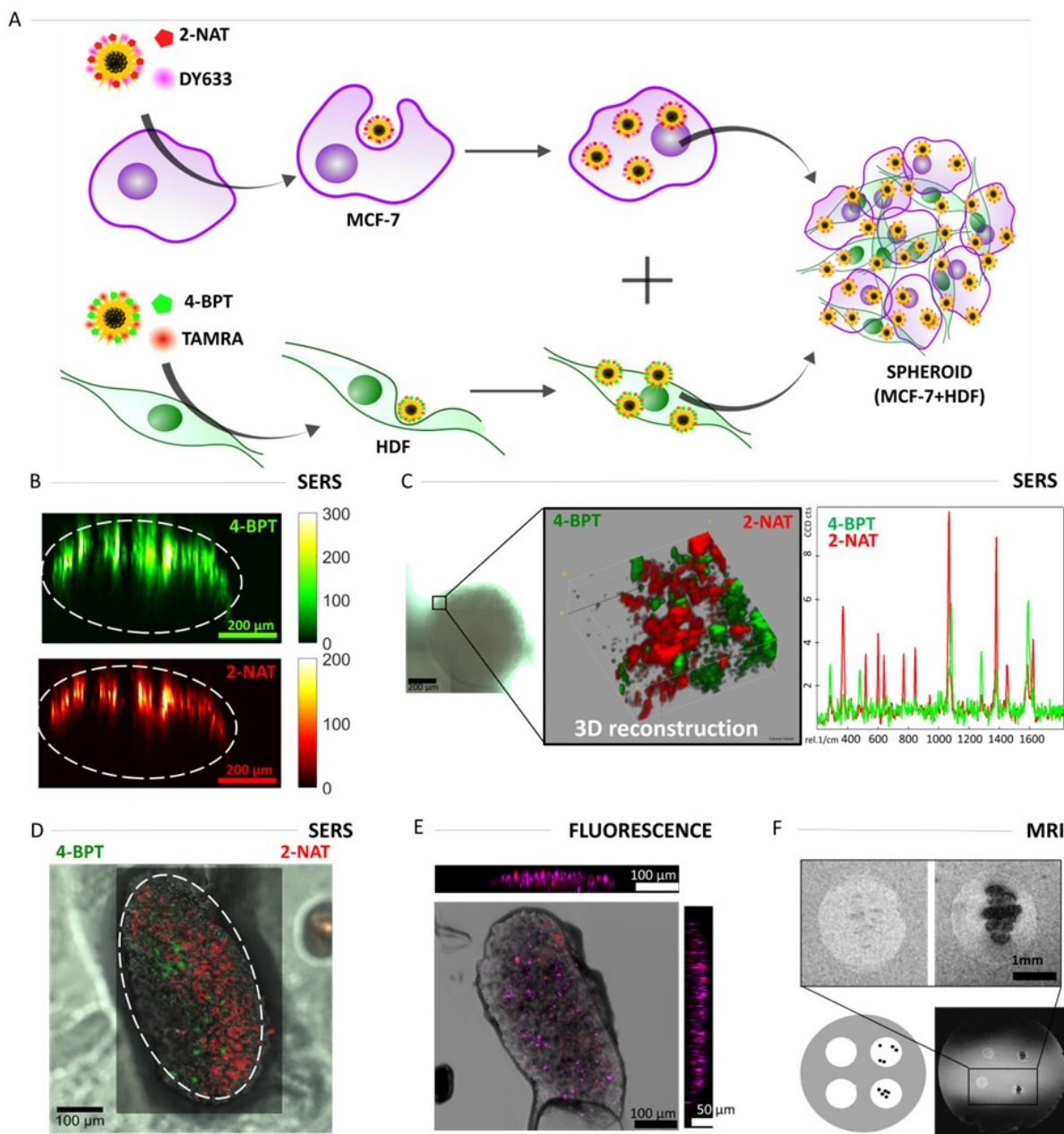
Figure 4. (A) Schematic illustration of spheroid preparation. MCF-7 and HDF cells were pre-incubated with IOAuNS@4-BPT@TAMRA and IOAuNS@2-NAT@DY633, respectively, prior to co-culture into the spheroid. **(B)** SERS mapping along the *xz* plane, of live spheroids showing pixels corresponding to 4-BPT (green) and 2-NAT (red). A total area of 800 x 430 μm² was imaged, with a resolution of 5 x 10 μm². Data were analyzed by Multiple Linear Regression Analysis (MLRA). The white dotted line highlights the edge of the spheroid **(C)** SERS mapping and 3D reconstruction of a selected volume at the outer edge of a live spheroid (brightfield image also shown). A total volume of 84 x 84 x 70 μm³ (*xyz*) was probed, with a resolution of 2 x 2 x 5 μm³ (*xyz*). Data were analyzed by TCA. **(D)** SERS map of a transversal cut (area 360 × 560 μm², 50 μm in thickness) of a fixed and embedded spheroid, showing the presence of 4-BPT and 2-NAT positive pixels throughout the *xy* plane**.** Data were analyzed by MLRA. **(E)** Orthogonal

projection collected by confocal fluorescence imaging of a transversal cut (50 µm in thickness) through a fixed and embedded spheroid. **(F)** MRI images from spheroids, with (right-hand side circles) and without (left-hand side circles) IOAuNS, planted in a phantom.

To mimic a more realistic situation, a second model of IOAuNS-spheroid interaction was developed. When NPs are administered *in vivo* for imaging purposes, NP penetration into the site of interest is determined by various factors, including the enhanced permeation and retention (EPR) effect, the tumor microvasculature, and potential spatial inhomogeneities in the NP delivery. We thus formed the spheroids first (again comprising MCF7 and HDF cells) and subsequently exposed them to a mixture of IOAuNS@BPT@TAMRA and IOAuNS@2NAT@DY633 (**Figure S21A**). Due to the size of IOAuNS, some sedimentation was observed during the studied period. To avoid this issue, we incubated IOAuNS with spheroids inside Eppendorf tubes, in a rotisserie rotator stored in an incubator at 37 ºC overnight. We first conducted confocal and SERS imaging of the whole live spheroid, again to determine IOAuNS distribution (**Figure S21B,C**). Similar results were observed as in the previous experiment, with limited capacity to determine the distribution of the NPs in deeper buried layers. Although it appeared that NPs were only located at the outer edge of the spheroids, this could only be confirmed by fixing and making a transversal cut along the *xy* plane. Indeed, SERS imaging clearly showed the presence of IOAuNS at the outer 100 µm layer of the spheroid, with no signal recorded from the inner core (**Figure S21D**). Thus, we proved that IOAuNSs are suitable contrast agents for spheroid imaging, and although they do penetrate the complex 3D model, a certain limitation was found in the light penetration depth that can be achieved.

Correlative imaging in an *ex vivo* model

In our pursuit of increasing complexity of the biological model, the next step comprised implementing the NP contrast agents for multimodal imaging in *ex vivo* models. For this purpose, we chose to conduct intracerebral injections into an excised mouse brain. The brain is an organ that provides a tissue with homogenous low-level background contrast in MRI and which is sufficiently large to apply multiple injections of different materials for comparison. Considering that we aimed at conducting SERS and fluorescence imaging on sliced tissue measuring a few tens of microns in thickness, MCF7 cells were chosen as the carriers of IOAuNS (using IOAuNS functionalized with 2-NAT and DY633 for SERS and fluorescence microscopy, respectively), because the injection of free IOAuNSs posed the problem of NPs diffusing into the tissue, inducing a significant reduction in SERS and fluorescence signals. First, MCF-7 cells were incubated overnight with IOAuNS@2-NAT@DY633, at a final total (Fe + Au) metal concentration of 0.05 mM, previously shown to be suitable for MRI imaging. Cells were trypsinized and concentrated to 2 x 10^6 cells/mL before injecting 5 µL into the right brain hemisphere. A second injection of IOAuNS@2-NAT@DY633, at the same estimated concentration in the cell-containing sample, was injected into the left hemisphere as a NP control. PBS buffer was also injected in the upper part of the brain as a media control. A schematic view of the layout is shown in **Figure 5A**. For MRI measurements, the entire brain was placed in the MRI scanner for imaging, whereas SERS and fluorescence images were obtained a posteriori, using the same brain tissue cut with a microtome. As can be clearly observed in **Figure 5B**, MRI imaging shows dark contrast where the injections were performed. Both free IOAuNS and IOAuNS-endocytosed MCF7 cells were visible in multiple slices (see **Figure S22**). Subsequently, SERS and fluorescence imaging of brain tissue cuts demonstrated

the suitability of these techniques for IOAuNS detection and mapping (**Figure 5C,D**). Whereas sample processing was arguably more complicated and laborious due to the numerous cuts to be made and sequential verification of positive signal, both techniques proved suitable for imaging of these multimodal NPs at different spatial resolutions and concentrations.
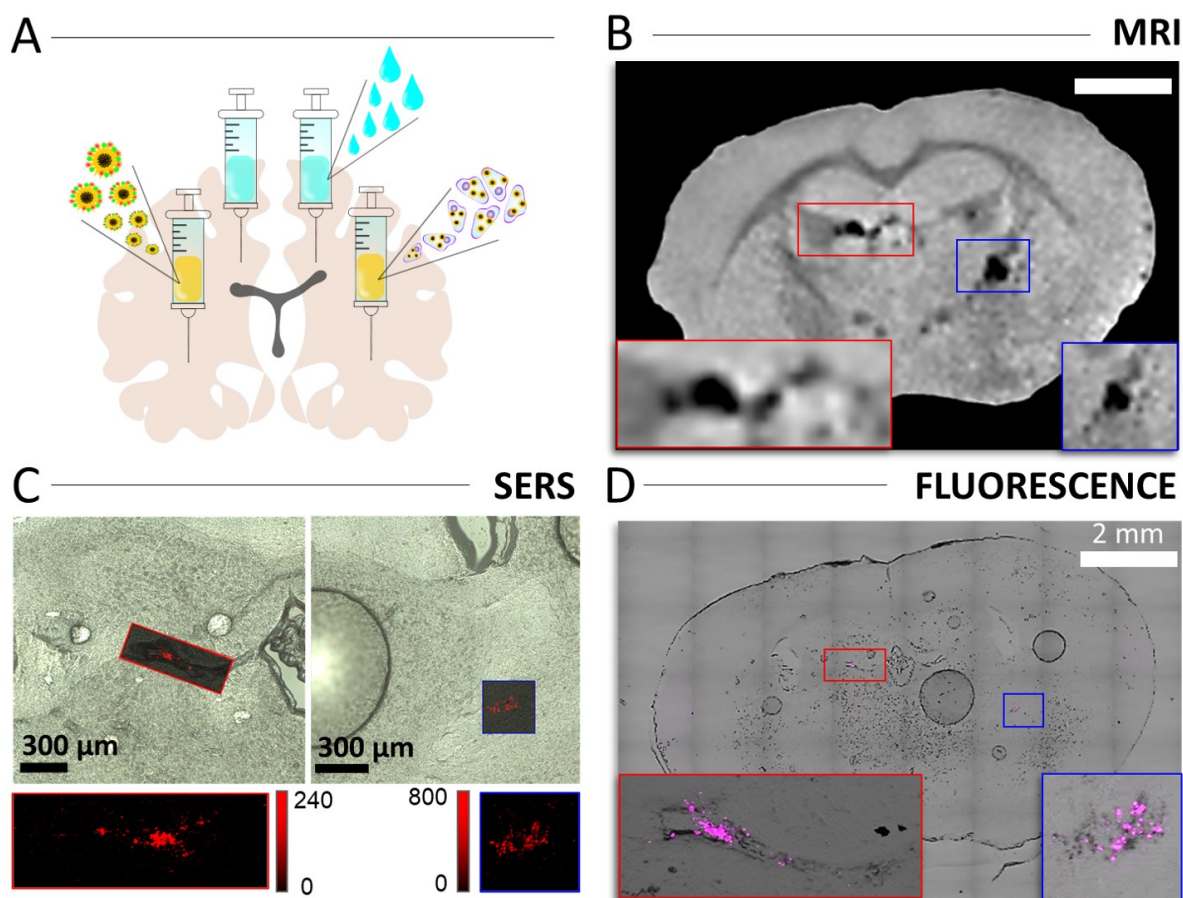
Figure 5. (A) Schematic illustration of different injections into a mouse brain, both with (right hemisphere; blue boxes in B-D) and without cells (left hemisphere; red boxes in B-D), as well as a PBS buffer control (top part of both left and right hemispheres). (**B-D**) Summary of results from MRI **(B)** SERS **(C)**, and fluorescence **(D)** imaging.

CONCLUSIONS

We have developed a colloidal system comprising hybrid NPs with magnetic and plasmonic components, which can act as contrast agents for multimodal imaging, combining SERS, MRI,

and fluorescence imaging. The NPs showed high versatility for imaging biological samples, ranging from 2D cell cultures to *ex vivo* models. We demonstrated that the overall particle size can be tuned by varying two key synthesis parameters, namely the concentration of gold spheres used as the nucleation points upon adsorption on iron oxide cores, and the added gold precursor for spike seeded growth. Through variation of these parameters, we achieved the fabrication of particles with different morphologies and sizes, which therefore display different optical properties. Whereas a low density of gold spheres on the surface of IONP cores leads to smaller final particles with incomplete gold shells and short tips, a higher Au NP density and higher concentration of $HAuCl_4$ in the seeded-growth reaction resulted in complete shell formation with well-defined spikes. The morphology of IOAuNS can thus be tuned accordingly and was optimized to obtain NPs with suitable properties for application in bioimaging. Whereas most published studies calculate the surface area of complex NPs for subsequent functionalization by assuming the volume of a sphere while using stars, we showed here a simple geometry model for realistic estimation of the surface area, which is more accurate toward efficient NP functionalization, while a better description of the surface morphology can be reached in compliment with 3D tomography data. We applied the results of this model to the surface functionalization of IOAuNS with Raman-active molecules and fluorescent dyes, and then demonstrated their non-cytotoxic nature in MCF7 breast cancer and fibroblast cells. With regards to the multimodal imaging properties of the IOAuNSs, SERS signal enhancement was found to be largely dependent on their absorbance and the density of hotspots (tips), so that the best candidates for SERS were smaller NPs with complete gold shells and well-defined spikes (IOAuNS bII). MRI experiments demonstrated that all particles provided T2 contrast due to the γ-Fe_2O_3 magnetic cores, regardless of the presence of any further SERS or fluorescence

functionalization. Furthermore, magnetic characterization of the NPs showed that the gold shell thickness did not affect the magnetic properties of the iron oxide cores. Both these aspects are particularly important for multimodal contrast agents, where the addition of one extra imaging component may hinder the efficacy of another. In summary, iron oxide-gold hybrid nanoparticles with controlled sizes were employed for SERS, MRI and fluorescence imaging within complex biological models. The synthesized IOAuNSs can thus be used as an interesting alternative to conventional contrast agents, achieving valuable information from each imaging technique that could improve the accuracy of the actual diagnostic methods. These findings open up the possibility of expanding the use of multimodal NPs for combination of imaging with photothermal therapy and magnetic targeting of cells and tissues, thus achieving theranostic and imaging with the same NPs.

AUTHOR INFORMATION

Corresponding Authors

*email addresses: djimenezdeaberasturi@cicbiomagune.es (D.J.A.);

llizmarzan@cicbiomagune.es (L.M.L.-M.)

Author Contributions

The manuscript was written through contributions of all authors. All authors have given approval to the final version of the manuscript.

Supporting Information. Additional characterization of IOAuNS, calculation of IOAuNS surface area, magnetic properties, polymer coating, SERS measurements, cellular uptake, cell

viability, MRI experiments in 2D cell models, characterization of 3D cell models and phantoms preparation.

REFERENCES

1. Ashammakhi, N.; Ahadian, S.; Darabi, M. A.; El Tahchi, M.; Lee, J.; Suthiwanich, K.; Sheikhi, A.; Dokmeci, M. R.; Oklu, R.; Khademhosseini, A. Minimally Invasive and Regenerative Therapeutics. *Adv. Mater.* **2019**, *31*, 1804041.

2. Louie, A. Multimodality Imaging Probes: Design and Challenges. *Chem. Rev.* **2010**, *110*, 3146–3195.

3. Lee, D. E.; Koo, H.; Sun, I. C.; Ryu, J. H.; Kim, K.; Kwon, I. C. Multifunctional Nanoparticles for Multimodal Imaging and Theragnosis. *Chem. Soc. Rev.* **2012**, *41*, 2656–2672.

4. Alvares, R. D. A.; Szulc, D. A.; Cheng, H. L. M. A Scale to Measure MRI Contrast Agent Sensitivity. *Sci. Rep.* **2017**, *7*, 15493.

5. Pierce, M. C.; Javier, D. J.; Richards-Kortum, R. Optical Contrast Agents and Imaging Systems for Detection and Diagnosis of Cancer. *Int. J. Cancer* **2008**, *123*, 1979–1990.

6. Hou, W.; Xia, F.; Alfranca, G.; Yan, H.; Zhi, X.; Liu, Y.; Peng, C.; Zhang, C.; de la Fuente, J. M.; Cui, D. Nanoparticles for Multi-Modality Cancer Diagnosis: Simple Protocol for Self-Assembly of Gold Nanoclusters Mediated by Gadolinium Ions. *Biomaterials* **2017**, *120*, 103–114.

7. Betzer, O.; Perets, N.; Angel, A.; Motiei, M.; Sadan, T.; Yadid, G.; Offen, D.; Popovtzer, R. In Vivo Neuroimaging of Exosomes Using Gold Nanoparticles. *ACS Nano* **2017**, *11*, 10883–10893.

8. Rastinehad, A. R.; Anastos, H.; Wajswol, E.; Winoker, J. S.; Sfakianos, J. P.; Doppalapudi, S. K.; Carrick, M. R.; Knauer, C. J.; Taouli, B.; Lewis, S. C.; Tewari, A. K.; Schwartz, J. A.; Canfield, S. E.; George, A. K.; West, J. L.; Halas, N. J. Gold Nanoshell-Localized Photothermal Ablation of Prostate Tumors in a Clinical Pilot Device Study. *Proc. Natl. Acad. Sci. U. S. A.* **2019**, *116*, 18590–18596.

9. Lenzi, E.; Jimenez de Aberasturi, D.; Liz-Marzán, L. M. Surface-Enhanced Raman Scattering Tags for Three-Dimensional Bioimaging and Biomarker Detection. *ACS Sens.* **2019**, *4*, 1126–1137.

10. Jimenez de Aberasturi, D.; Serrano-Montes, A. B.; Langer, J.; Henriksen-Lacey, M.; Parak, W. J.; Liz-Marzán, L. M. Surface Enhanced Raman Scattering Encoded Gold Nanostars for Multiplexed Cell Discrimination. *Chem. Mater.* **2016**, *28*, 6779–6790.

11. García-Astrain, C.; Lenzi, E.; Jimenez de Aberasturi, D.; Henriksen-Lacey, M.; Binelli, M. R.; Liz-Marzán, L. M. 3D-Printed Biocompatible Scaffolds with Built-In Nanoplasmonic Sensors. *Adv. Funct. Mater.* **2020**, *30*, 2005407.

12. Reguera, J.; Jiménez De Aberasturi, D.; Henriksen-Lacey, M.; Langer, J.; Espinosa, A.; Szczupak, B.; Wilhelm, C.; Liz-Marzán, L. M. Janus Plasmonic-Magnetic Gold-Iron

Oxide Nanoparticles as Contrast Agents for Multimodal Imaging. *Nanoscale* **2017**, *9*, 9467–9480.

13. Zhou, Z.; Yang, L.; Gao, J.; Chen, X. Structure–Relaxivity Relationships of Magnetic Nanoparticles for Magnetic Resonance Imaging. *Adv. Mater.* **2019**, *31*, 1804567.

14. Wang, G.; Gao, W.; Zhang, X.; Mei, X. Au Nanocage Functionalized with Ultra-Small Fe_3O_4 Nanoparticles for Targeting T1-T2 Dual MRI and CT Imaging of Tumor. *Sci. Rep.* **2016**, *6*, 28258.

15. Zeng, J.; Gong, M.; Wang, D.; Li, M.; Xu, W.; Li, Z.; Li, S.; Zhang, D.; Yan, Z.; Yin, Y. Direct Synthesis of Water-Dispersible Magnetic/Plasmonic Heteronanostructures for Multimodality Biomedical Imaging. *Nano Lett.* **2019**, *19*, 3011–3018.

16. Wang, W.; Hao, C.; Sun, M.; Xu, L.; Xu, C.; Kuang, H. Spiky Fe_3O_4@Au Supraparticles for Multimodal in Vivo Imaging. *Adv. Funct. Mater.* **2018**, *28*, 1800310.

17. Jeon, M.; Halbert, M. V.; Stephen, Z. R.; Zhang, M. Iron Oxide Nanoparticles as T1 Contrast Agents for Magnetic Resonance Imaging: Fundamentals, Challenges, Applications, and Prospectives. *Adv. Mater.* **2020**, *33*, 1906539.

18. Quintanilla, M.; Henriksen-lacey, M.; Renero-Lecuna, C.; Liz-Marzán, L. M. Challenges for Optical Nanothermometry in Biological Environments. *Chem. Soc. Rev.* **2022**, *51*, 4223-4242.

19. Kouhpanji, M. R. Z.; Stadler, B. J. H. A Guideline for Effectively Synthesizing and Characterizing Magnetic Nanoparticles for Advancing Nanobiotechnology: A Review. *Sensors* **2020**, *20*, 2554.

20. Li, J.; Hu, Y.; Yang, J.; Wei, P.; Sun, W.; Shen, M.; Zhang, G.; Shi, X. Hyaluronic Acid-Modified Fe_3O_4 at Au Core/Shell Nanostars for Multimodal Imaging and Photothermal Therapy of Tumors. *Biomaterials* **2015**, *38*, 10–21.

21. Hou, X.; Wang, X.; Liu, R.; Zhang, H.; Liu, X.; Zhang, Y. Facile Synthesis of Multifunctional Fe_3O_4@SiO_2@Au Magneto-Plasmonic Nanoparticles for MR/CT Dual Imaging and Photothermal Therapy. *RSC Adv.* **2017**, *7*, 18844–18850.

22. Tomitaka, A.; Arami, H.; Ahmadivand, A.; Pala, N.; McGoron, A. J.; Takemura, Y.; Febo, M.; Nair, M. Magneto-Plasmonic Nanostars for Image-Guided and NIR-Triggered Drug Delivery. *Sci. Rep.* **2020**, *10*, 10115.

23. Hemery, G.; Keyes, A. C.; Garaio, E.; Rodrigo, I.; Garcia, J. A.; Plazaola, F.; Garanger, E.; Sandre, O. Tuning Sizes, Morphologies, and Magnetic Properties of Monocore versus Multicore Iron Oxide Nanoparticles through the Controlled Addition of Water in the Polyol Synthesis. *Inorg. Chem.* **2017**, *56*, 8232–8243.

24. Mehdipour, M.; Gloag, L.; Lian, J.; Tilley, R. D.; Gooding, J. J. Zero-Valent Iron Core-Iron Oxide Shell Nanoparticles Coated with Silica and Gold with High Saturation Magnetization. *Chem. Commun.* **2021**, *57*, 13142–13145.

25. Kolosnjaj-Tabi, J.; Javed, Y.; Lartigue, L.; Volatron, J.; Elgrabli, D.; Marangon, I.; Pugliese, G.; Caron, B.; Figuerola, A.; Luciani, N.; Pellegrino, T.; Alloyeau, D.; Gazeau, F. The One Year Fate of Iron Oxide Coated Gold Nanoparticles in Mice. *ACS Nano* **2015**, *9*, 7925–7939.

26. Gavilán, H.; Sánchez, E. H.; Brollo, M. E. F.; Asín, L.; Moerner, K. K.; Frandsen, C.; Lázaro, F. J.; Serna, C. J.; Veintemillas-Verdaguer, S.; Morales, M. P.; Gutiérrez, L.

Formation Mechanism of Maghemite Nanoflowers Synthesized by a Polyol-Mediated Process. *ACS Omega* **2017**, *2*, 7172–7184.

27. Jana, N. R.; Gearheart, L.; Murphy, C. J. Seeding Growth for Size Control of 5-40 nm Diameter Gold Nanoparticles. *Langmuir* **2001**, *17*, 6782–6786.

28. Zou, F.; Ding, Q.; Tran, V. T.; Wang, G.; Zhang, Y.; Kang, S.; Lee, J.; Zhou, H. Magnetically Recyclable Catalytic Activity of Spiky Magneto-Plasmonic Nanoparticles. *RSC Adv.* **2015**, *5*, 56653–56657.

29. Pellegrino, T.; Manna, L.; Kudera, S.; Liedl, T.; Koktysh, D.; Rogach, A. L.; Keller, S.; Radler, J.; Natile, G.; Parak, W. J. Hydrophobic Nanocrystals Coated with an Amphiphilic Polymer Shell: A General Route to Water Soluble Nanocrystals. *Nano Lett.* **2004**, *4*, 703–707.

30. Jimenez de Aberasturi, D.; Henriksen-Lacey, M.; Litti, L.; Langer, J.; Liz-Marzán, L. M. Using SERS Tags to Image the Three-Dimensional Structure of Complex Cell Models. *Adv. Funct. Mater.* **2020**, *30*, 1909655.

31. Lenzi, E.; Henriksen-lacey, M.; Molina, B.; Langer, J.; de Albuquerque, C. D. L.; Jimenez de Aberasturi, D.; Liz-Marzán, L. M. Combination of Live Cell Surface-Enhanced Raman Scattering Imaging with Chemometrics to Study Intracellular Nanoparticle Dynamics. *ACS Sens.* **2022**, *7*, 1747-1756.

32. Lartigue, L.; Hugounenq, P.; Alloyeau, D.; Clarke, S. P.; Lévy, M.; Bacri, J. C.; Bazzi, R.; Brougham, D. F.; Wilhelm, C.; Gazeau, F. Cooperative Organization in Iron Oxide Multi-Core Nanoparticles Potentiates Their Efficiency as Heating Mediators and MRI Contrast Agents. *ACS Nano* **2012**, *6*, 10935–10949.

33. Turkevich, J. Colloidal Gold. Part I - Historical and Preparative Aspects, Morphology and Structure. *Gold Bull.* **1985**, *18*, 86–91.

34. Bertuit, E.; Benassai, E.; Meriguet, G.; Greneche, J. M.; Baptiste, B.; Neveu, S.; Wilhelm, C.; Abou-Hassan, A. Structure-Property-Function Relationships of Iron Oxide Multicore Nanoflowers in Magnetic Hyperthermia and Photothermia. *ACS Nano* **2022**, *16*, 271–284.

35. Shafi, K. V. P. M.; Ulman, A.; Dyal, A.; Yan, X.; Yang, N. L.; Estournès, C.; Fournès, L.; Wattiaux, A.; White, H.; Rafailovich, M. Magnetic Enhancement of γ-Fe$_2$O$_3$ Nanoparticles by Sonochemical Coating. *Chem. Mater.* **2002**, *14*, 1778–1787.

36. Kucheryavy, P.; He, J.; John, V. T.; Maharjan, P.; Spinu, L.; Goloverda, G. Z.; Kolesnichenko, V. L. Superparamagnetic Iron Oxide Nanoparticles with Variable Size and an Iron Oxidation State as Prospective Imaging Agents. *Langmuir* **2013**, *29*, 710–716.

37. Yadav, B. Sen; Singh, R.; Vishwakarma, A. K.; Kumar, N. Facile Synthesis of Substantially Magnetic Hollow Nanospheres of Maghemite (γ-Fe$_2$O$_3$) Originated from Magnetite (Fe$_3$O$_4$) via Solvothermal Method. *J. Supercond. Nov. Magn.* **2020**, *33*, 2199–2208.

38. Serrano-Montes, A. B.; Jimenez de Aberasturi, D.; Langer, J.; Giner-Casares, J. J.; Scarabelli, L.; Herrero, A.; Liz-Marzán, L. M. A General Method for Solvent Exchange of Plasmonic Nanoparticles and Self-Assembly into SERS-Active Monolayers. *Langmuir* **2015**, *31*, 9205–9213.

39. Rodríguez-Lorenzo, L.; Alvarez-Puebla, R. A.; Pastoriza-Santos, I.; Mazzucco, S.; Stéphan, O.; Kociak, M.; Liz-Marzán, L. M.; García de Abajo, F. J. Zeptomol Detection

through Controlled Ultrasensitive Surface-Enhanced Raman Scattering. *J. Am. Chem. Soc.* **2009**, *131*, 4616–4618.

40. LaConte, L. E. W.; Nitin, N.; Zurkiya, O.; Caruntu, D.; O'Connor, C. J.; Hu, X.; Bao, G. Coating Thickness of Magnetic Iron Oxide Nanoparticles Affects R2 Relaxivity. *J. Magn. Reson. Imaging* **2007**, *26*, 1634–1641.

41. Zhou, H.; Tang, J.; Li, J.; Li, W.; Liu, Y.; Chen, C. In Vivo Aggregation-Induced Transition between T1 and T2 Relaxations of Magnetic Ultra-Small Iron Oxide Nanoparticles in Tumor Microenvironment. *Nanoscale* **2017**, *9*, 3040–3050.

42. Wang, Y.; Li, X.; Chen, P.; Dong, Y.; Liang, G.; Yu, Y. Enzyme-Instructed Self-Aggregation of Fe_3O_4 Nanoparticles for Enhanced MRI T2 Imaging and Photothermal Therapy of Tumors. *Nanoscale* **2020**, *12*, 1886–1893.

43. Costa, E. C.; Moreira, A. F.; de Melo-Diogo, D.; Gaspar, V. M.; Carvalho, M. P.; Correia, I. J. 3D Tumor Spheroids: An Overview on the Tools and Techniques Used for Their Analysis. *Biotechnol. Adv.* **2016**, *34*, 1427–1441.

44. Pulagam, K. R.; Henriksen-Lacey, M.; B. Uribe, K.; Renero-Lecuna, C.; Kumar, J.; Charalampopoulou, A.; Facoetti, A.; Protti, N.; Gómez-Vallejo, V.; Baz, Z.; Kumar, V.; Sánchez-Iglesias, A.; Altieri, S.; Cossío, U.; Di Silvio, D.; Martínez-Villacorta, A. M.; Ruiz de Angulo, A.; Rejc, L.; Liz-Marzán, L. M.; Llop, J. In Vivo Evaluation of Multifunctional Gold Nanorods for Boron Neutron Capture and Photothermal Therapies. *ACS Appl. Mater. Interfaces* **2021**, *13*, 49589–49601.

TOC Graphic

HYBRID NPs

4-BPT
2-NAT

TAMRA
DY633

SERS   MRI   FLUORESCENCE
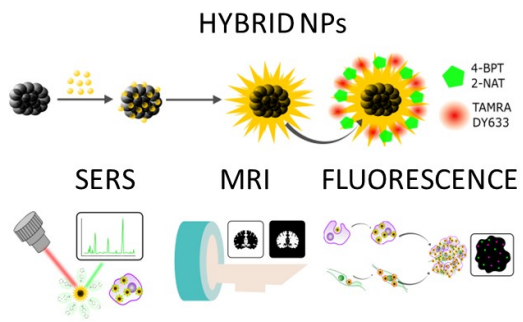
SUPPORTING INFORMATION

Hybrid Magnetic-Plasmonic Nanoparticle Probes For Multimodal Bioimaging

Cristina de la Encarnación [1,2], Elisa Lenzi[1,3], Malou Henriksen-Lacey[1,3], Beatriz Molina[1,4], Kellie Jenkinson[5], Ada Herrero[1,3], Lorena Colás[1], Pedro Ramos-Cabrer [1,6], Jhoan Toro-Mendoza[1], Iñaki Orue[7], Judith Langer[1,3], Sara Bals[5], Dorleta Jimenez de Aberasturi[1,3,6], and Luis M. Liz-Marzán[1,3,6*]*

[1] CIC biomaGUNE, Basque Research and Technology Alliance (BRTA), 20014, San Sebastián, Spain

[2] Department of Applied Chemistry, University of the Basque Country, 20018 Donostia-San Sebastián, Spain

[3] Centro de Investigación Biomédica en Red, Bioingeniería, Biomateriales y Nanomedicina (CIBER-BBN), 20014, San Sebastián, Spain

[4] Current address: Biobide Spain, Paseo Mikeletegi 56 Bajo, 20009 Donostia-San Sebastián, Spain

[5] EMAT and NANOlab Center of Excellence -University of Antwerp, 2020 Antwerp, Belgium

[6] Ikerbasque, Basque Foundation for Science, 48009, Bilbao, Spain

[7] SGIKER, Servicios Generales de Investigación, University of the Basque Country, 48940 Leioa, Spain

*Corresponding authors' email: djimenezdeaberasturi@cicbiomagune.es (D.J.A.); llizmarzan@cicbiomagune.es (L.M.L.-M.)

Table S1: Concentration of AuNPs solution (25 mL) used for the fabrication of the IOAuNPs used as seeds for the tip's growth

[Au] of AuNPs solution	Seeds for IOAuNSs
0.1 mM	a; I, II, III, IV
0.05 mM	b; I, II, III, IV
0.02 mM	c; I, II, III, IV

Table S2: Summary of the reactants used for the synthesis of IOAuNSs

Sample	Total Vol. (mL)	HAuCl$_4$ (µL) (0.129 mM)	HCl (µL) (1 M)	IOAuNPs (µL) [Au] = 0.30 mM	AgNO$_3$ (µL) (3 mM)	Ascorbic acid (µL) (100 mM)	PEG (µL) (1 mM)
aI	10	5	2.5	25	175	25	30
aII	10	10	5.0	25	350	50	30
aIII	10	15	7.5	25	525	75	30
aIV	10	20	10	25	700	100	30

Sample	Total Vol. (mL)	HAuCl$_4$ (µL) (0.129 mM)	HCl (µL) (1 M)	IOAuNPs (µL) [Au] = 0.20 mM	AgNO$_3$ (µL) (3 mM)	Ascorbic acid (µL) (100 mM)	PEG (µL) (1 mM)
bI	10	5	2.5	35	175	25	30
bII	10	10	5.0	35	350	50	30
bIII	10	15	7.5	35	525	75	30
bIV	10	20	10	35	700	100	30

Sample	Total Vol. (mL)	HAuCl$_4$ (µL) (0.129 mM)	HCl (µL) (1 M)	IOAuNPs (µL) [Au] = 0.10 mM	AgNO$_3$ (µL) (3 mM)	Ascorbic acid (µL) (100 mM)	PEG (µL) (1 mM)
cI	10	5	2.5	70	175	25	30
cII	10	10	5.0	70	350	50	30
cIII	10	15	7.5	70	525	75	30
cIV	10	20	10	70	700	100	30
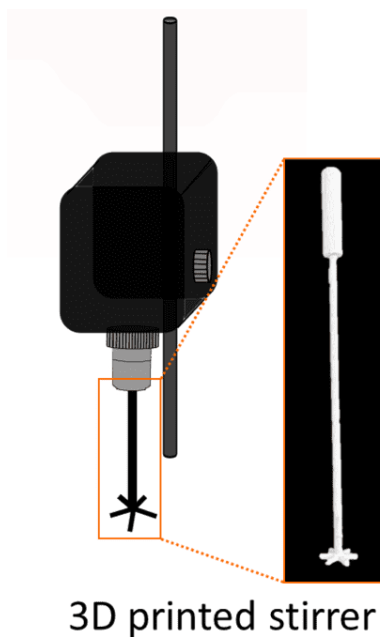
3D printed stirrer

Figure S1. Polylactic acid (PLA) 3D printed stirrer that worked attached to a mechanical stirrer
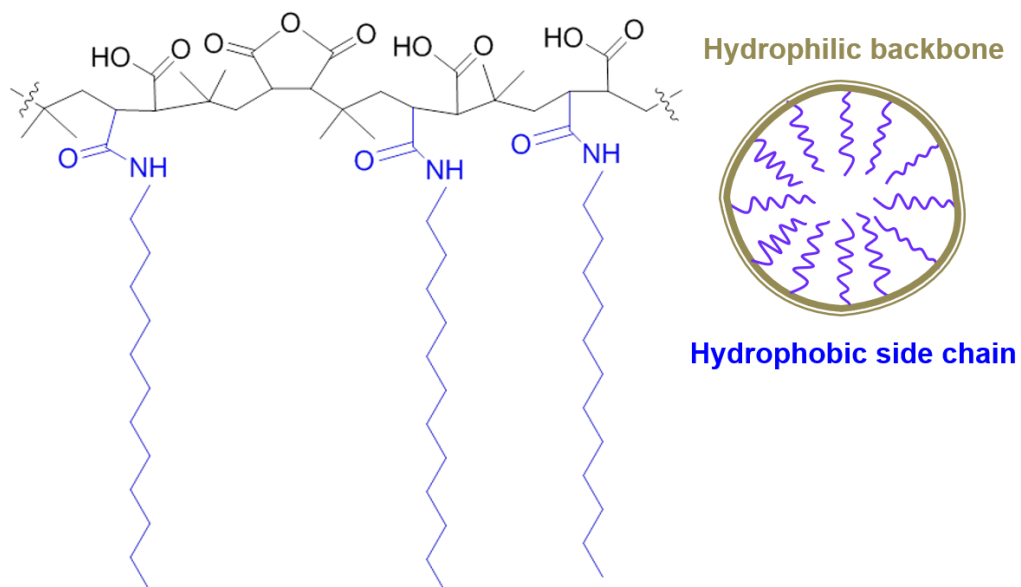
Figure S2. Structure of the amphiphilic polymer (PMA). The hydrophilic backbone of polyisobutylene-alt-maleic anhydride (black) is modified via amide bonds with hydrophobic dodecylamine side chains (blue). A sketch of the amphiphilic polymer is shown in the right panel. Figure modified from ref. 1.
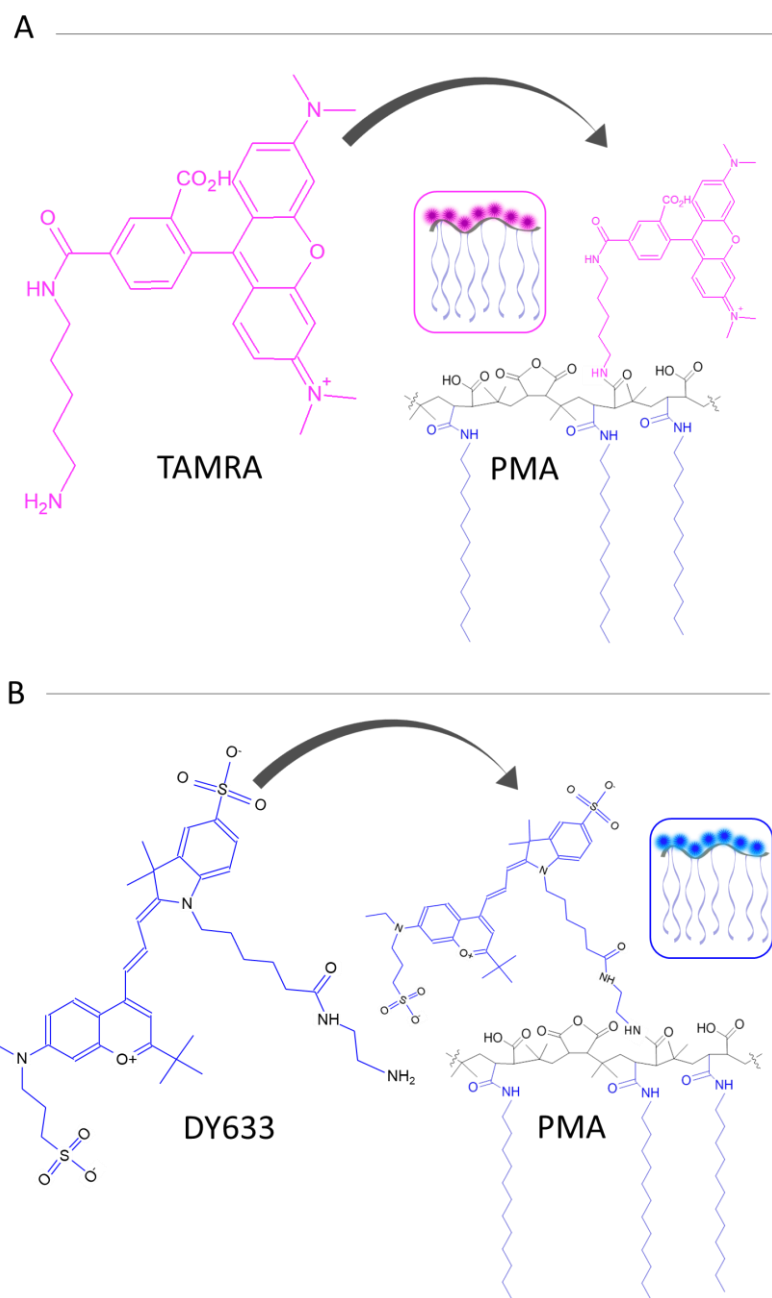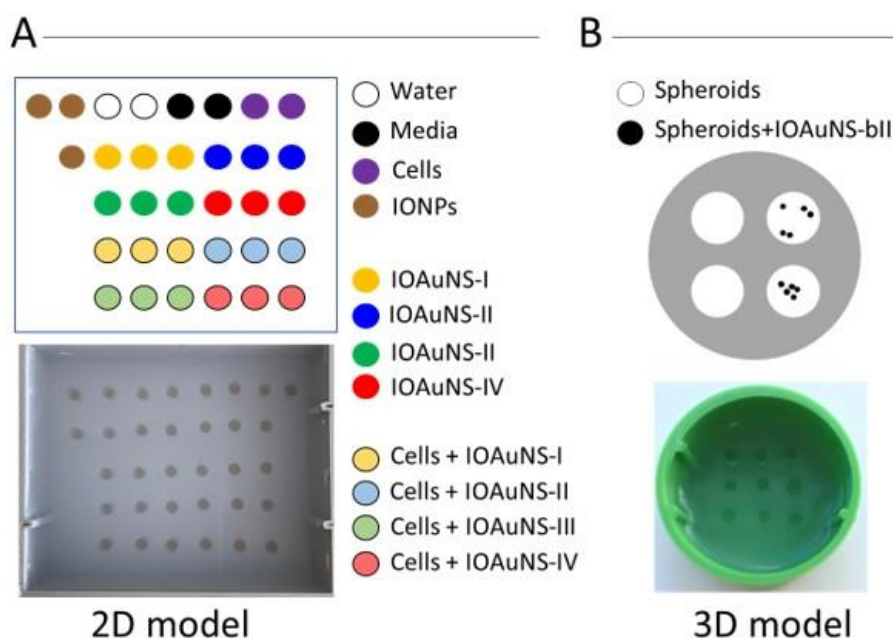
Figure S3. Structure of TAMRA **(A)** and DY633 **(B)** and scheme of PMA modification with the dyes via amide bonds to the carboxylic group of the hydrophilic backbone of the PMA (black). Figure modified from ref. 2.
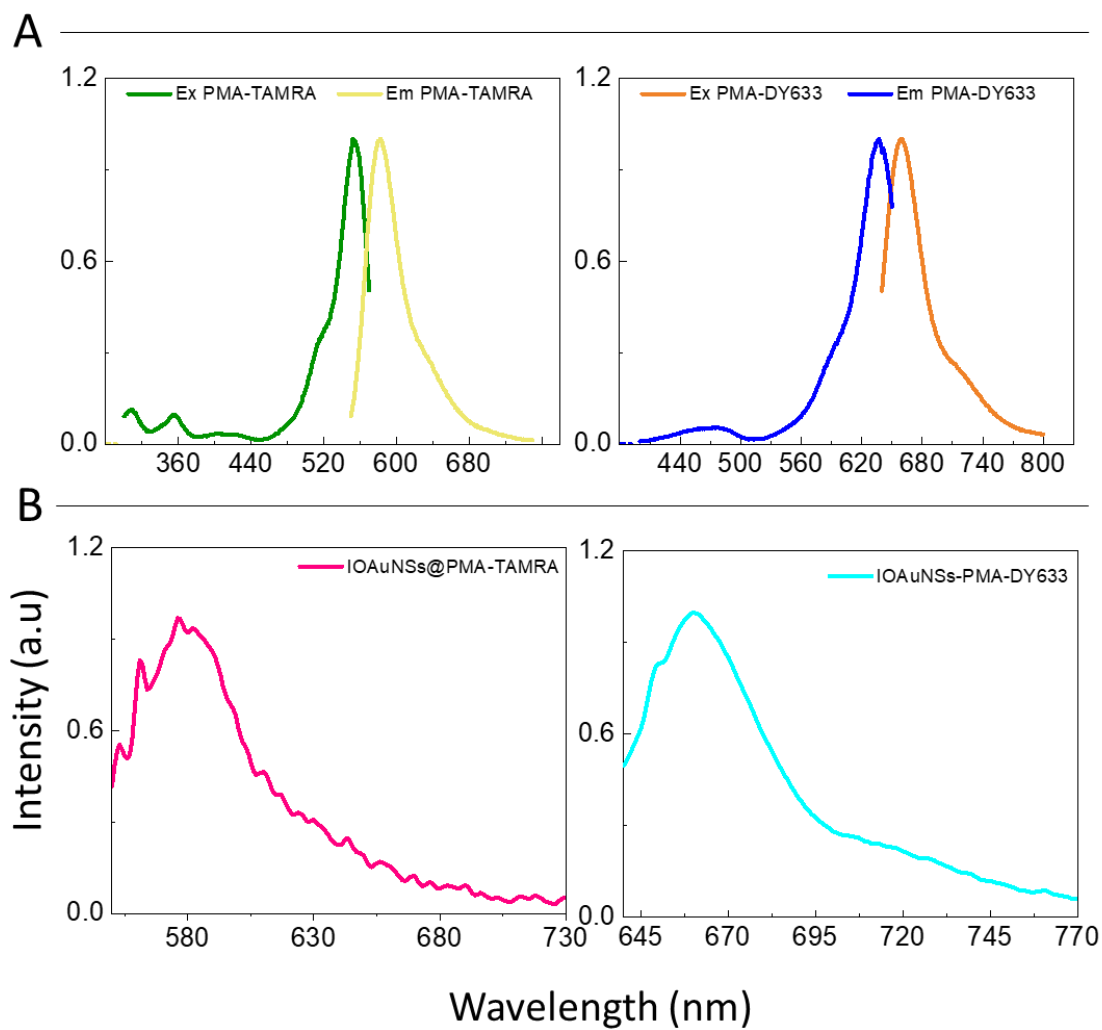
Figure S4. Normalized fluorescence excitation and emission spectra of PMA-TAMRA and PMA-DY633 micelles **(A)**. Normalized fluorescence emission spectra of IOAuNS@4-BPT@TAMRA (pink) and IOAuNS@2-NAT@DY633 (blue) NPs **(B).**

Table S3. Concentrations used for the preparations of phantoms for MRI, measured by ICP-MS.

	IOAuNS [Au] µM	Cells+IOAuNS [Au] µM
aI	47	9
aII	48	7.8
aIII	35	40
aIV	33	10
bI	28	26
bII	49	32
bIII	36	38
bIV	35	17
cI	29	36
cII	38	31
cIII	23	7
cIV	25	7

Figure S5: Scheme of the phantom model and distribution of samples and controls used in the phantom model for MRI measurements on 2D **(A)** and 3D **(B)** cell models.
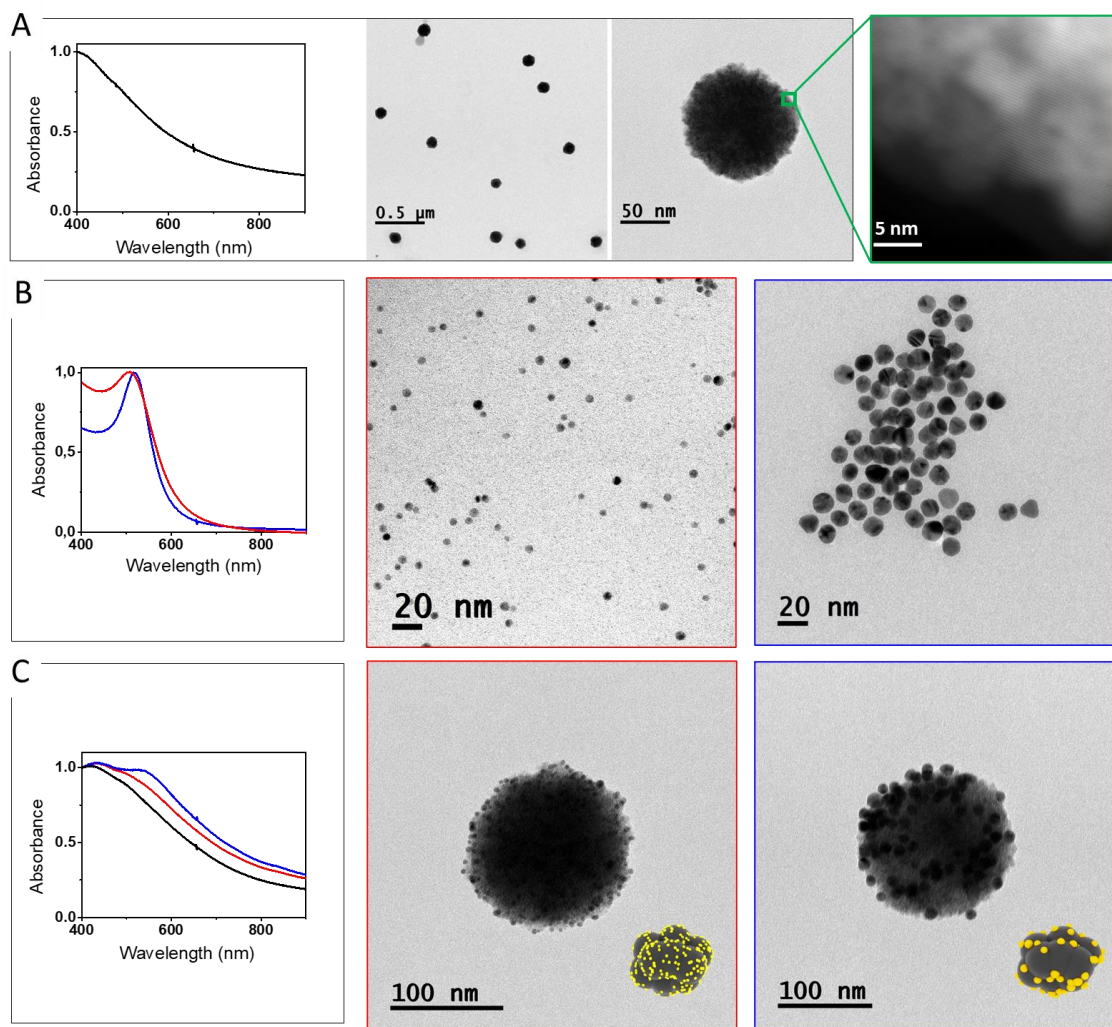
Figure S6. Normalized UV-Vis-NIR spectra and TEM images of the various NPs used for IOAuNS synthesis: **(A)** IONPs (a HRTEM image of 5 nm crystallites is shown in the green box); **(B)** AuNPs with average diameters of 4 nm (red; λ_{max} = 510 nm) and 15 nm (blue; λ_{max} = 520 nm). **(C)** IONPs decorated with 4 nm (red) and 15 nm (blue) gold spheres. The insets depict schematic representations of the structures. The black spectrum in **(C)** corresponds to IONPs as a control. All spectra were normalized at 400 nm.
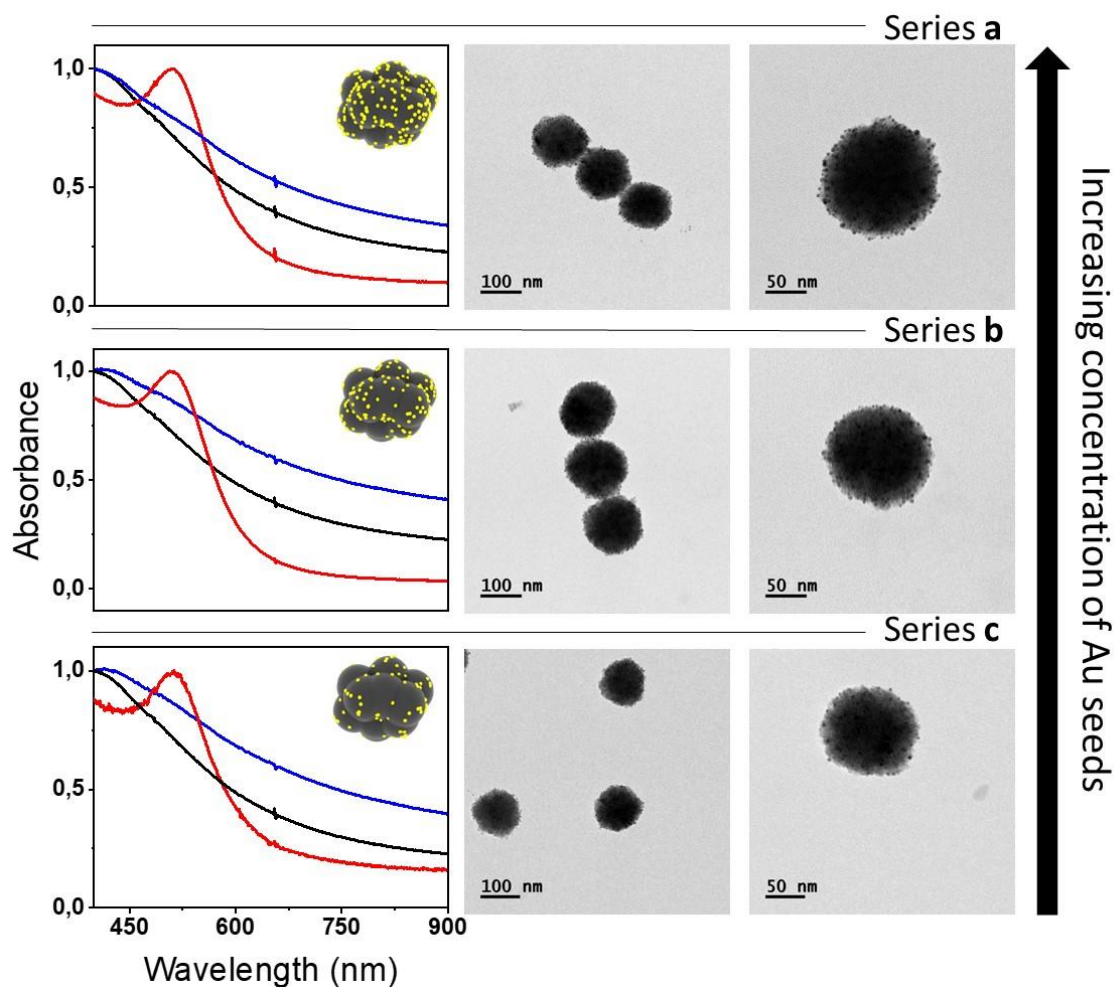
Figure S7. Normalized UV-vis-NIR spectra and TEM images of series a-c of 4 nm AuNPs (red), IONPs (black), and IONPs decorated with AuNPs (IOAuNPs) (blue). The insets in the left column depict the schematic representation of each nanostructure. The [Au]/[Fe] ratio decreases from series a = 3.7×10^{-2} to series b = 1.1×10^{-2} to series c = 2.3×10^{-3}. All spectra were normalized at 400 nm.
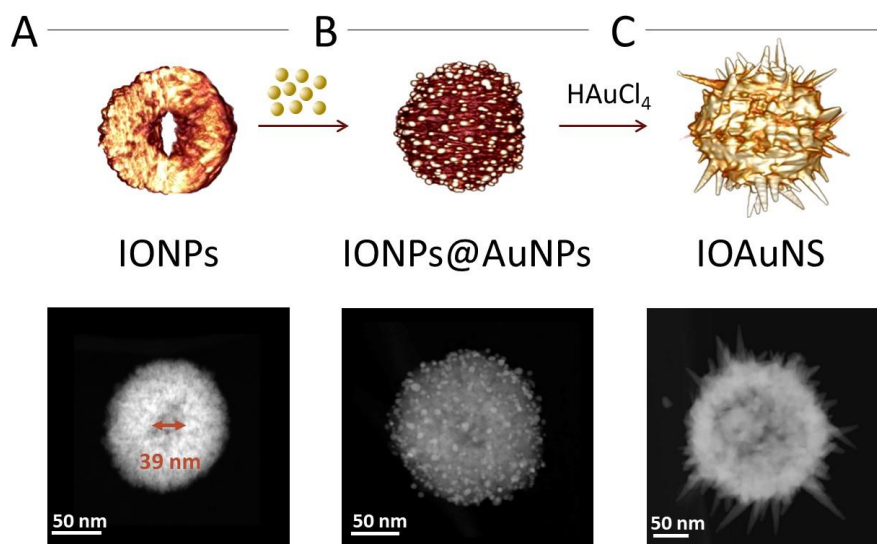
Figure S8. Top: Electron tomography reconstructions of IONP **(A)**, IONP@AuNP **(B)** and IOAuNS **(C)**. Bottom: Corresponding ADF-STEM images.
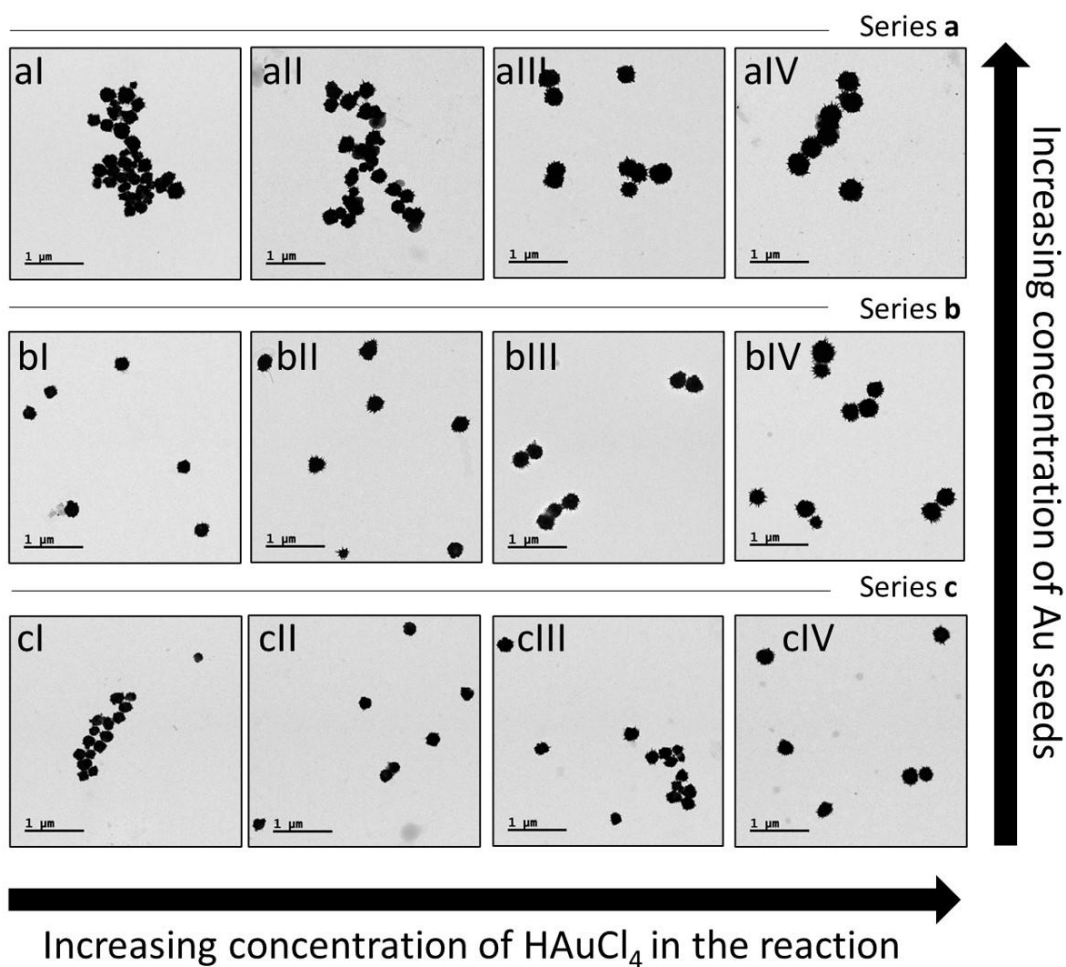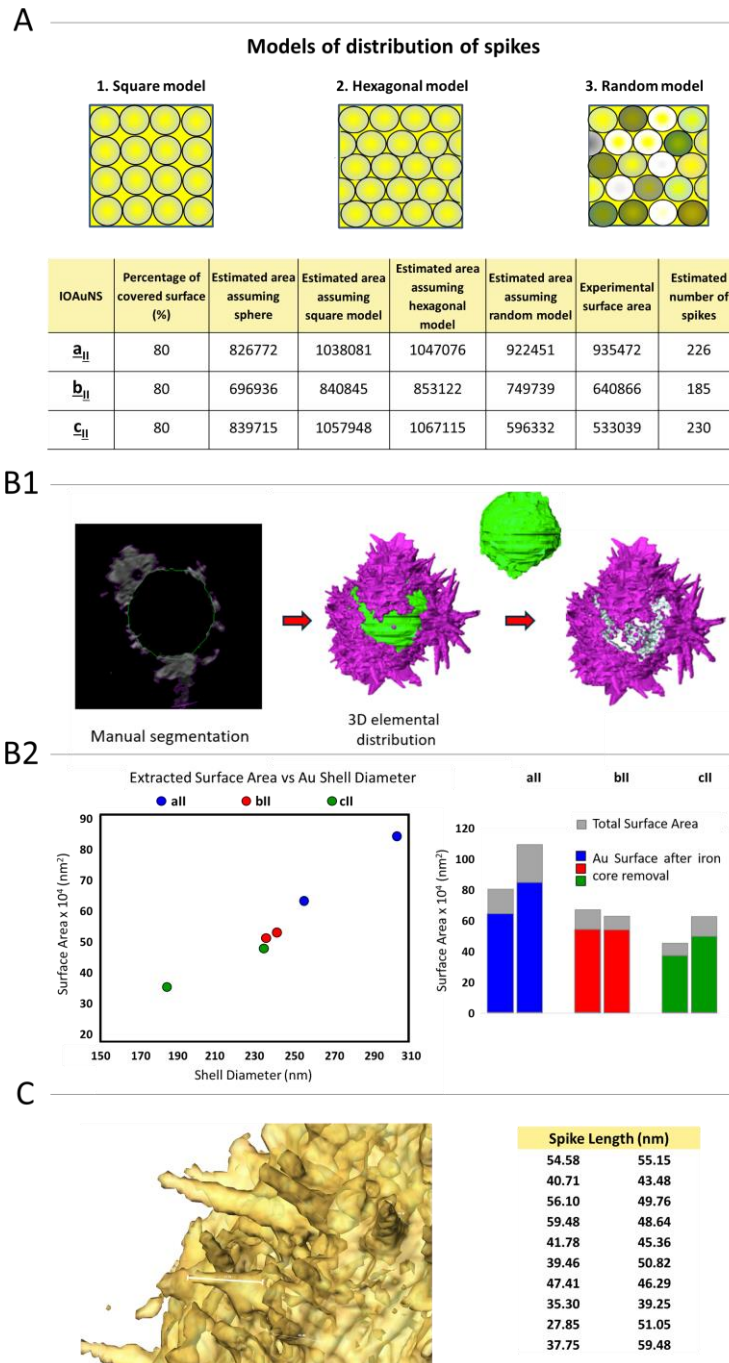

Figure S9. Low magnification TEM images of IOAuNS with varying size and shape. Decreasing concentrations of gold seeds were used for particles from series **a** through **c,** whereas HAuCl₄ concentration was increased from **I** to **IV** in each series.

Table S4. Size measurements of IOAuNS from TEM images. Sizes decrease from series **a** to **b** to **c.**

Diameter measured by TEM (nm)			
aI	**aII**	**aIII**	**aIV**
285.6 ± 22.4	334.9 ± 32.9	372.4 ± 32.1	436.3 ± 35.1
bI	**bII**	**bIII**	**bIV**
257.9 ± 25.2	281.5 ± 21.5	328.4 ± 35.2	404.2 ± 36.1
cI	**cII**	**cIII**	**cIV**
169.3 ± 20.1	266.2 ± 25.8	282.3 ± 30.4	315.2 ± 30.1
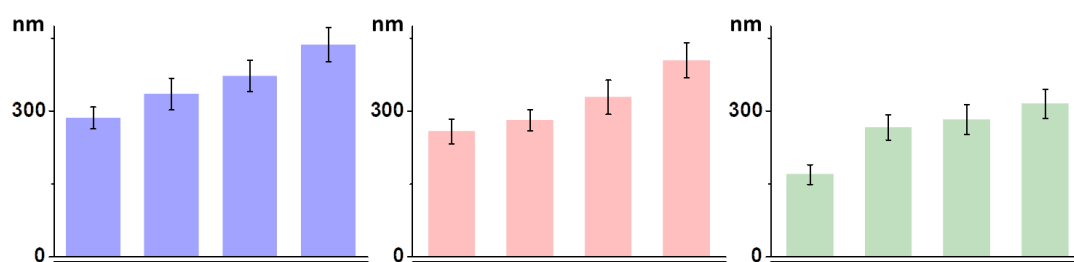
Figure S10. Graphical representation of the results from TEM determination of particle diameter, listed in Table S4.

A

Models of distribution of spikes

1. Square model   2. Hexagonal model   3. Random model

IOAuNS	Percentage of covered surface (%)	Estimated area assuming sphere	Estimated area assuming square model	Estimated area assuming hexagonal model	Estimated area assuming random model	Experimental surface area	Estimated number of spikes
a_{II}	80	826772	1038081	1047076	922451	935472	226
b_{II}	80	696936	840845	853122	749739	640866	185
c_{II}	80	839715	1057948	1067115	596332	533039	230

B1

Manual segmentation   3D elemental distribution

B2

Extracted Surface Area vs Au Shell Diameter

    ● aII   ● bII   ● cII

aII   bII   cII

□ Total Surface Area
■ Au Surface after iron core removal

C

Spike Length (nm)	
54.58	55.15
40.71	43.48
56.10	49.76
59.48	48.64
41.78	45.36
39.46	50.82
47.41	46.29
35.30	39.25
27.85	51.05
37.75	59.48

Figure S11. (A) Three scenarios for spike distribution, modeled as fully ordered circles (base of conical spikes) on a surface, assuming that the cone radius is much smaller that the radius of the core sphere. In the table, the data obtained from the theoretical models are compared to the experimental data. All the area values are given in nm^2. **(B1)** Sketch of the procedure to calculate Au coverage, comprising removal of the iron core by manual segmentation in 3D ADF-STEM images (see Methods). **(B2)** Analysis of shell diameter and total Au surface area for the particles in series II. **(C)** Spike length distribution for particle bII, obtained from the 3D reconstruction of a single NP.

Description of geometrical models: We assumed spikes with conical shape (height L; base radius B), much smaller than the radius of the spherical core R_{core}. We can thus assume the core as a flat surface, with area $A_{core} = 4\pi R_{core}^2 = l_{core}^2$ ($l_{core} = 2R_{core}\sqrt{\pi}$ is the side of a square with the same area as the sphere). The area of the conical spike is $A_{spike} = \pi B(\sqrt{L^2 + B^2})$.

Three different arrangements were considered: first, a square array of *n* circles with equal radius (**Figure S11A**), $n = N^2 = \left(l_{core}/2B\right)^2 = \pi \left(R_{core}/B\right)^2$. The total surface area is the sum of the cones (spikes) plus the total free area, given by:

$$A_{TNS} = N\left[\pi B\sqrt{L^2 + B^2} + l_{squa}^2 - \pi B^2\right]$$

A second case comprises a hexagonal arrangement of identical conical spikes on a planar area, covering an area φ of ca. 0.9069. The area occupied by the circular bases of the spikes is $4\pi R_{core}^2 \varphi = n\pi B^2$, so that: $n = \frac{4\pi\varphi R_{core}^2}{\pi B^2} = 4\varphi \left(\frac{R_{core}}{B}\right)^2$. Hence, the total area of an IOAuNS with a hexagonal surface arrangement of conical spikes is:

$$A_{TNS} = 4\pi R_{core}^2 (1 - \varphi) + n\left[\pi B(\sqrt{L^2 + B^2})\right]$$

The third model involves a hexagonal arrangement of conical spikes with a random distribution of lengths fitting the experimental data for IOAuNS surface (from electron tomography). The number and area of the spikes, as well as the total IOAuNS surface area, was estimated from all three models, the random model being the most realistic one.
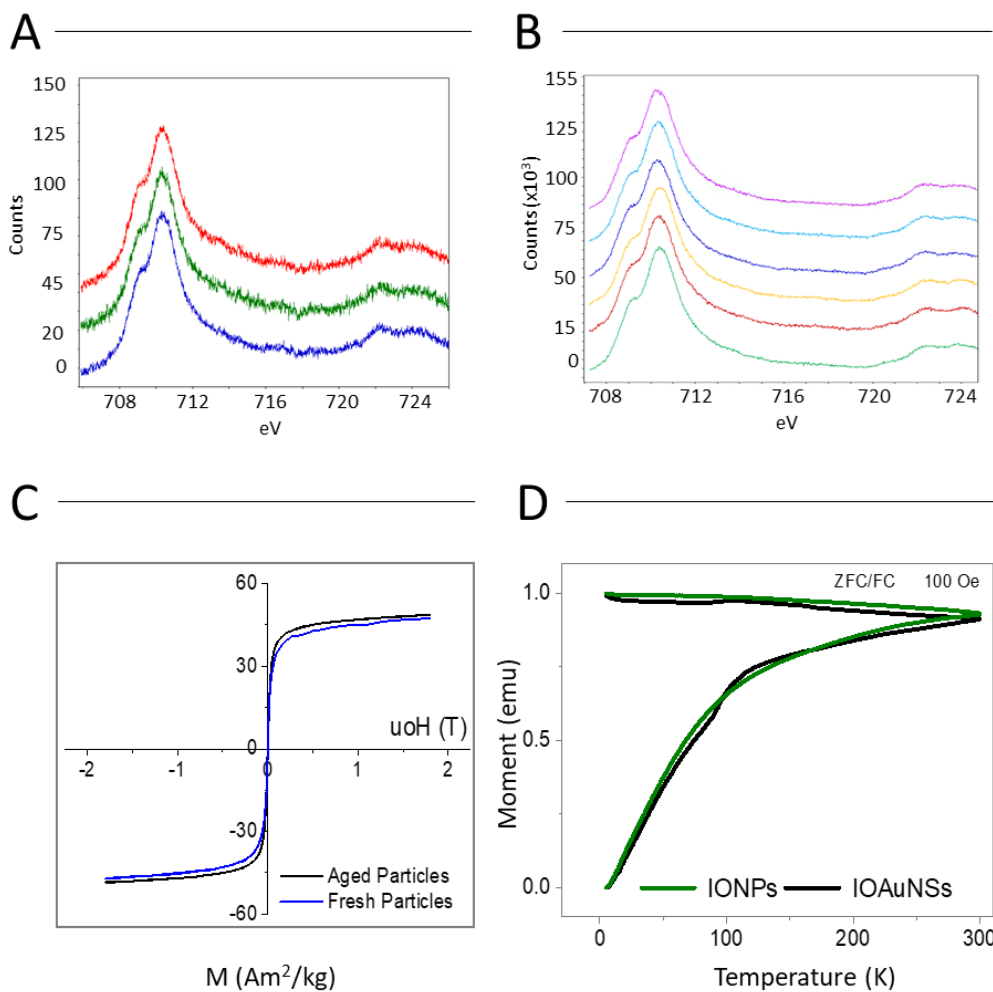
Figure S12. **(A)** EELS spectra of freshly prepared IONPs, showing a low shoulder centered at 710.8 eV, assigned to Fe^{3+}. **(B)** EELS spectra of IONPs that were aged for 6 months. **(C)** Hysteresis loops for freshly made (blue) and aged (black) IONPs. **(D)** ZFC/FC curves for IONPs (green) and IOAuNSs (black), recorded at a magnetic field of 100 Oe.

For EELS analysis, energy losses corresponding to maghemite and magnetite[3] were used as references and IONPs were analyzed in different areas, within the same nanoparticle. The most notable difference between maghemite (Fe_2O_3) and magnetite (Fe_3O_4) is the shift of the main peak containing a small shoulder centered around 710.8 eV, assigned to Fe^{3+}.

Table S5. Raman shifts of the characteristic vibrations in solution and in cells for 4-BPT and 2-NAT, and assignment of their Raman-active vibrational modes.

| RaR	vib v ~ / cm^{-1} (in solution)	vib v ~ / cm^{-1} (in cell)	mode assignment
4-BPT	1084	1083	ring C-H bend[4,5]
	1285	1284	ring C-C stretch[4,5]
	1593/1604	1593/1603	ring C-C stretch[4,5]
2-NAT	640	641	ring deformation[6]
	769	770	ring deformation[6]
	846	850	C-H twist[6]
	1070	1070	ring C-H bend (in plane)[6]
	1383	1382	ring C-C stretch[6]
	1453	1454	ring C-C stretch[6]
	1586	1587	ring C-C stretch[6]
	1626	1625	ring C-C stretch[6]
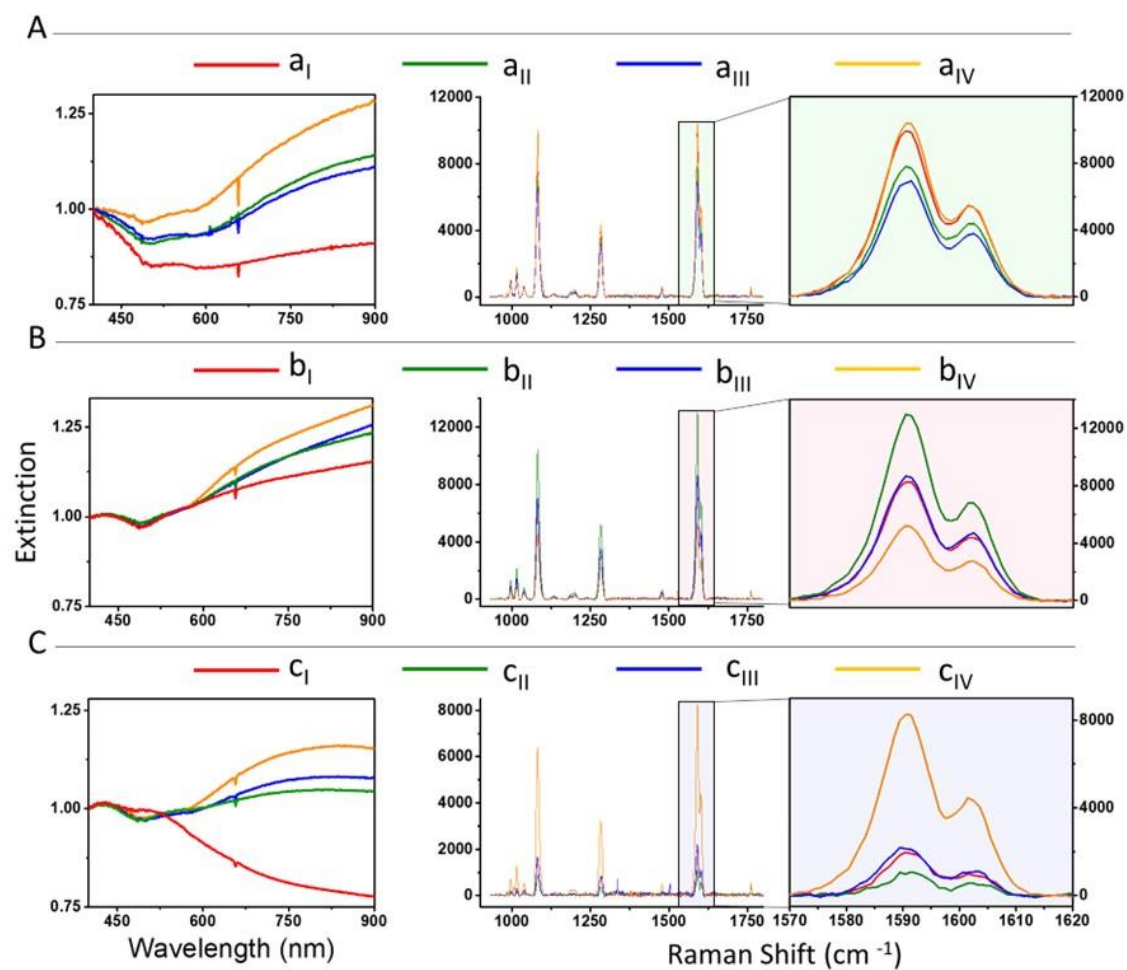
Figure S13. Normalized UV-vis-NIR spectra (left) for IOAuNSs after coating with 4-bisphenylthiol (4-BPT). SERS spectra (centre and right) of PMA-encapsulated IOAuNPs. Colour scheme for all IOAuNSs: series I (red), series II (green), series III (blue), and series IV (yellow). All samples were measured in solution and at the same iron concentration [Fe = 0.1 mM].
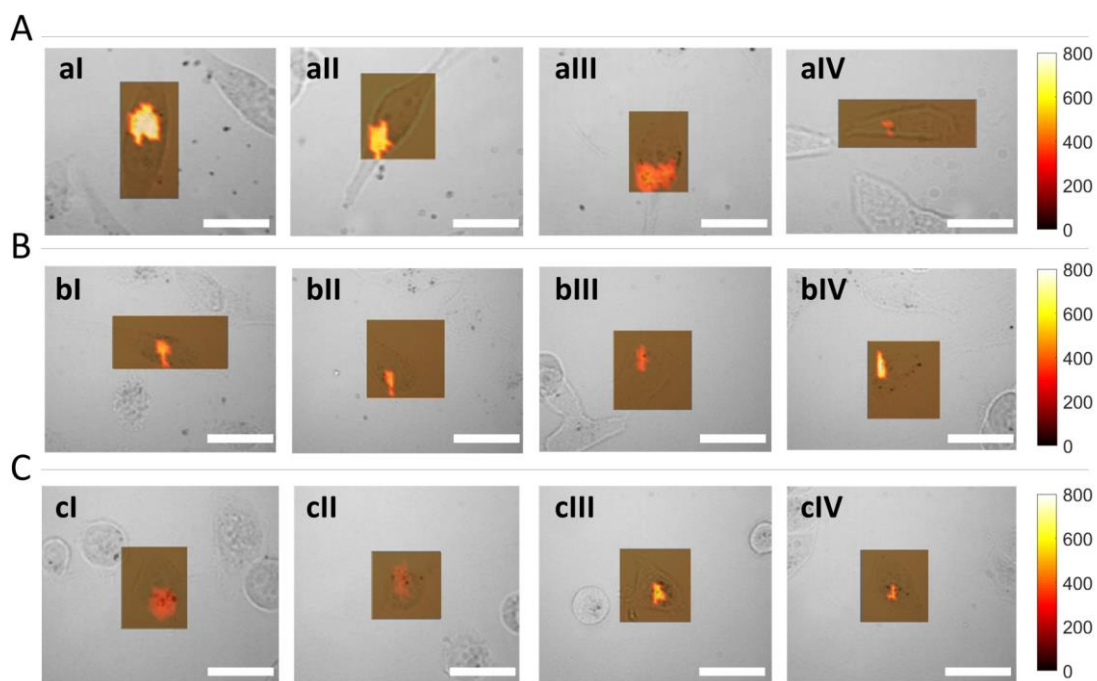
**Figure S14.** SERS maps of MCF7 cells (area $30 \times 30 \ \mu m^2$), pre-loaded with IOAuNS@4-BPT from series a-c, and I-IV. Multiple Linear Regression analysis was performed on the data to obtain the regression coefficient calculated as b-values, whose intensities indicate the presence of the IOAuNPs inside the cell area. The scale bars correspond to 20 μm.
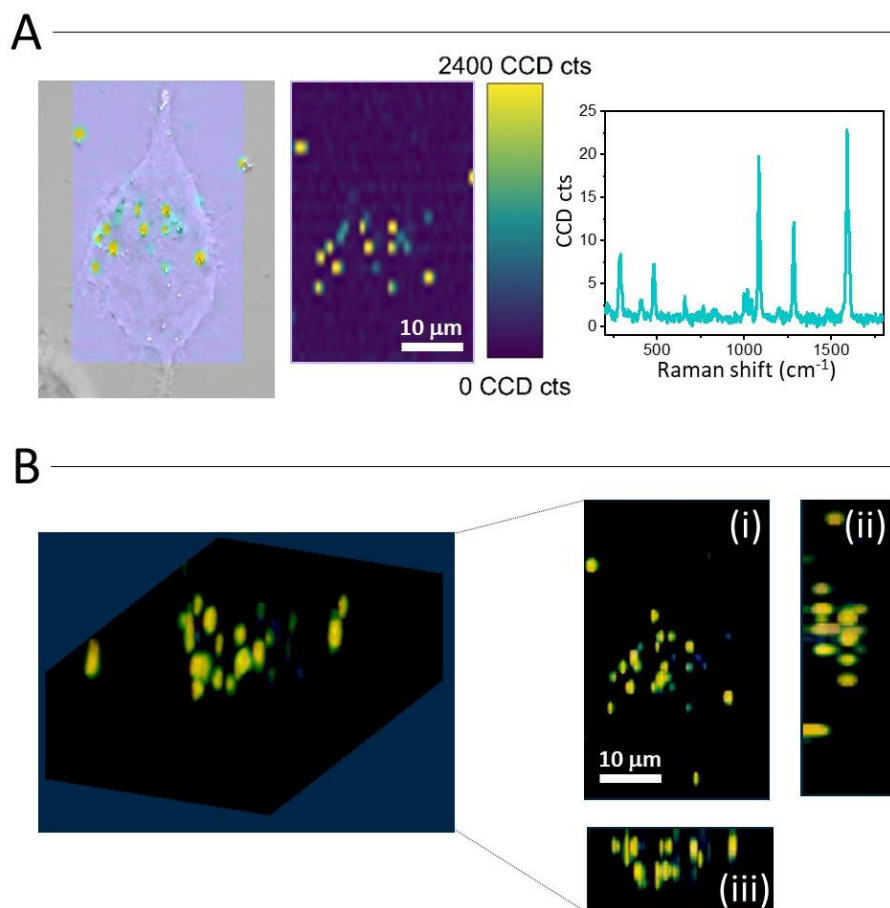
Figure S15. (A) SERS map (left) analyzed with true component analysis which evidence in an intensity color code the presence of the NPs and representative SERS spectrum (right) of a single cell pre-loaded with IOAuNS@4-BPT-bII. **(B)** 3D Reconstruction of the measurement shown in **(A).** Orthogonal projections of a z-stack are shown in the right panel, including *xy* projection (i) *yz* projection (ii) and *xz* projection (iii).
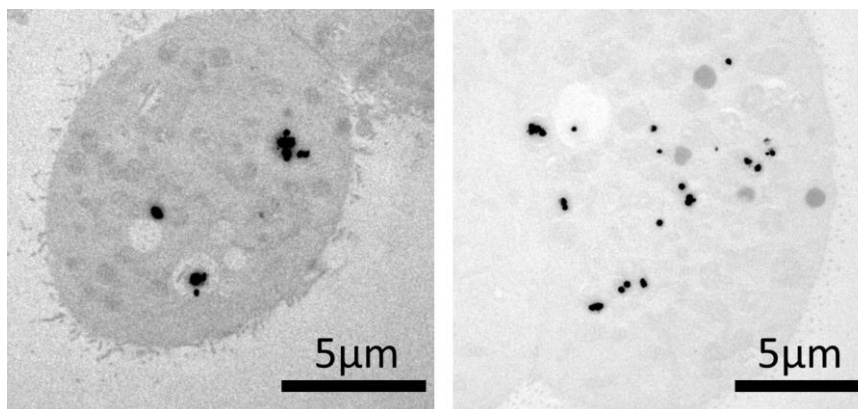
Figure S16. TEM images of ultramicrotomed MCF7 cells containing IOAuNS confined in endosomes.
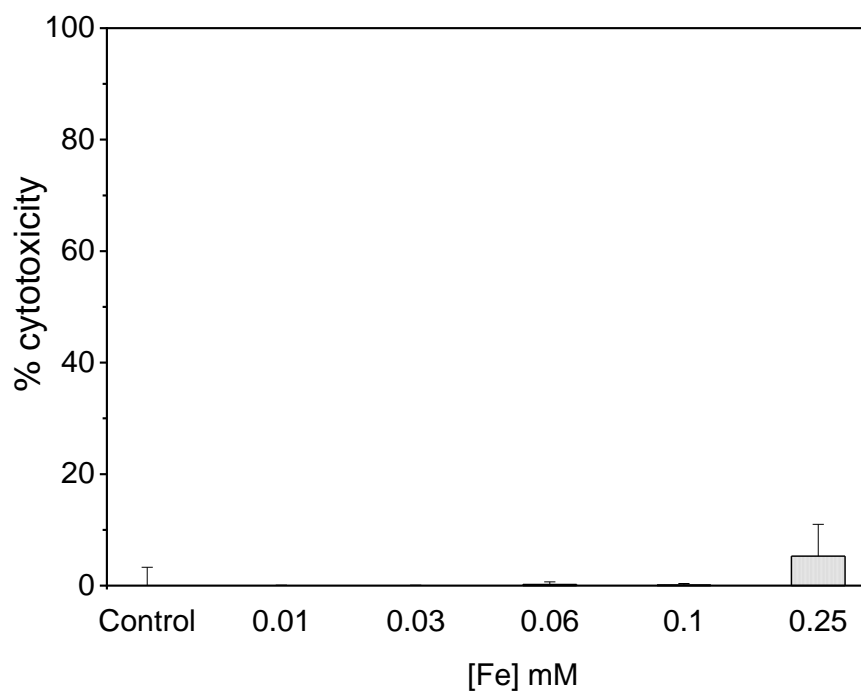

Figure S17. Results of LDH tests after incubation of MCF-7 cells with IOAuNS-bII, for 48 hours.
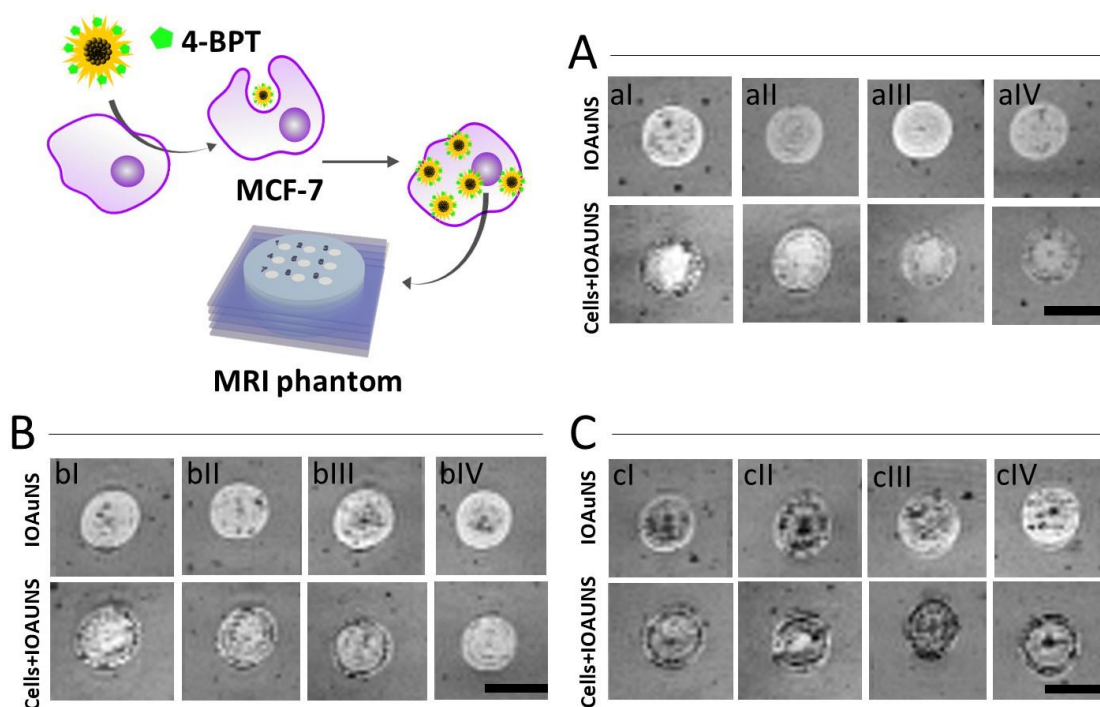
Figure S18. MRI experiments in 2D using agarose phantoms (see methods). **(A)** IOAuNSs (I, II, III and IV) of the series a were placed in the holes in solution (upper part) and internalized in MCF7 cells (lower part). Likewise, IOAuNSs from series b and c are represented in **(B)** and **(C)** respectively in the figure. Scale bar: 2 mm.
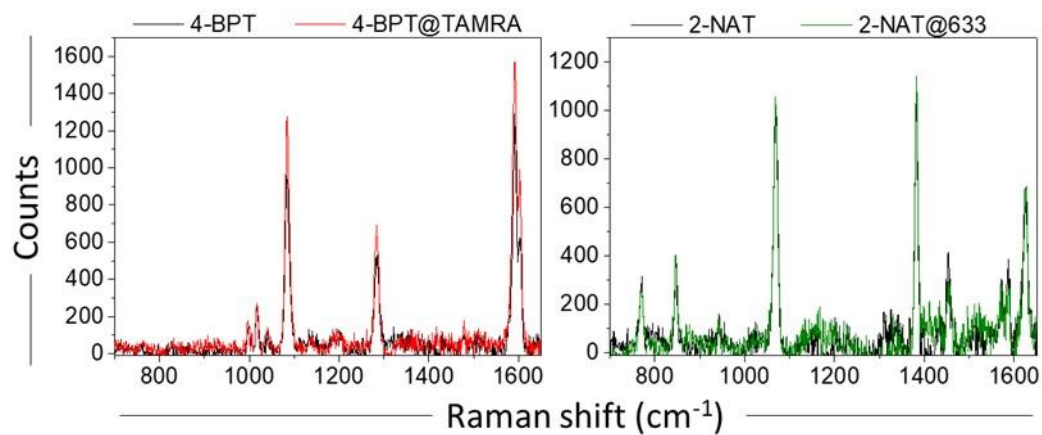

Figure S19. SERS spectra of IOAuNS labeled with Raman reporters and fluorescent dyes, compared to those of IOAuNS labeled with Raman reporters only. The concentration was fixed to [Au+Fe] = 0.5 mM. No significant changes were appreciated, neither in the vibrational fingerprint of the Raman tags nor in the signal intensity.
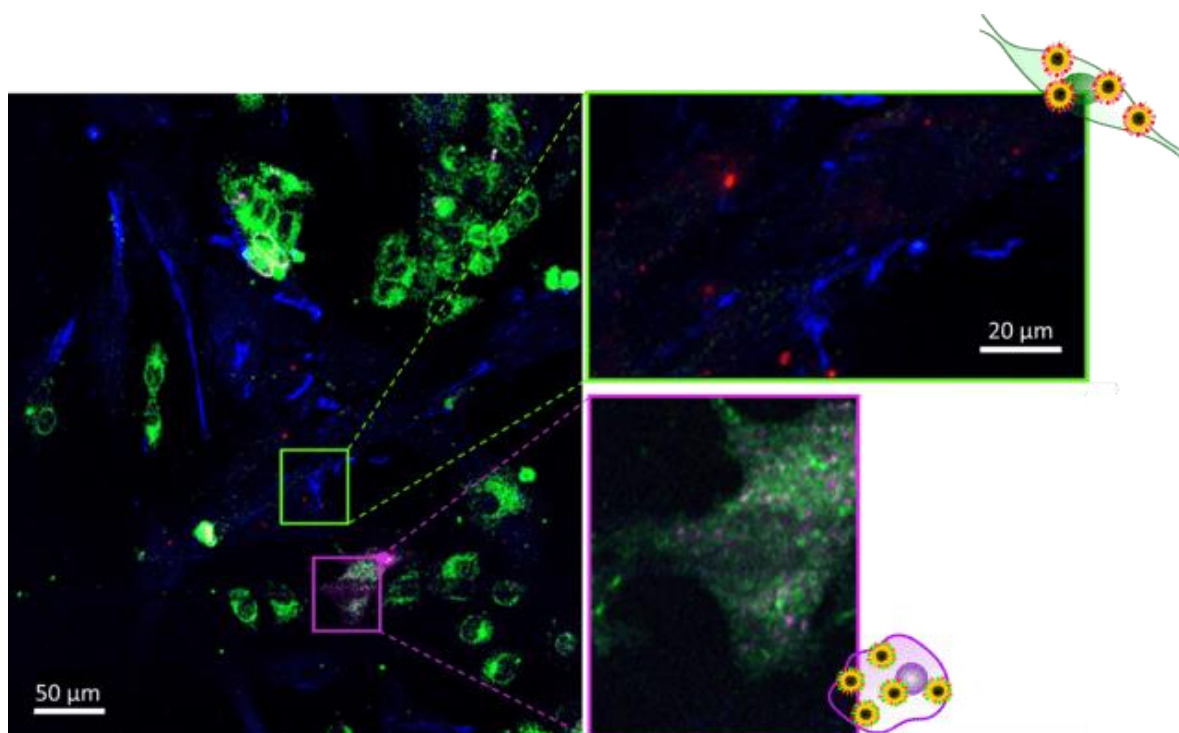
Figure S20. Cellular uptake of IOAuNSs. Immunostaining of MCF7 (E-cadherin, green) and HDF (TE-7, blue) cells previously incubated with IOAuNS@4-BPT@TAMRA (red) and IOAuNS@2-NAT@DY633 (pink), respectively.
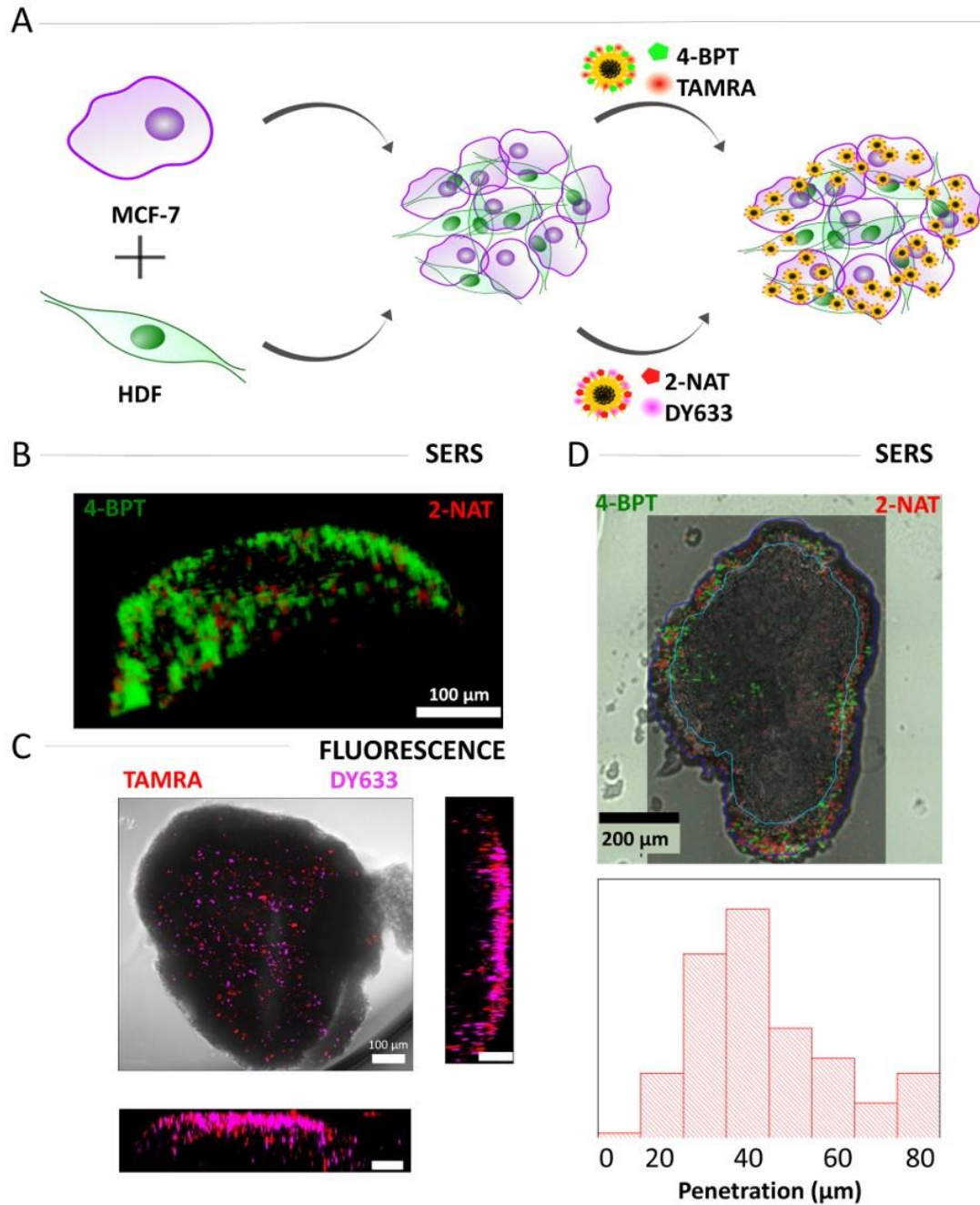
Figure S21. (A) Illustration of spheroid formation. **(B)** SERS imaging of a MCF7:HDF spheroid incubated with IOAuNS@4-BPT@TAMRA (in green) and IOAuNS@2-NAT@Dy633 (in red) NPs. A volume of 400 x 380 x 150 μm^3 was mapped and MLRA used to obtain b-values whose intensities are shown. Scale bar, 100 μm **(C)** Orthogonal projection captured using confocal fluorescence imaging of a *z*-stack of a MCF7:HDF spheroid incubated with IOAuNS@4-BPT@TAMRA (in red) and IOAuNS@2-NAT@Dy633 (in pink) NPs. Scale bars correspond to 100 μm **(D)** Brightfield image with overlaid SERS map of IOAuNS@4-BPT@TAMRA (in green) and IOAuNS@2-NAT@Dy633 (in red) NPs, detected in an OCT-embedded slice (635 × 875 μm^2)of MCF7:HDF spheroid. MLRA used to obtain b-values whose intensities are shown. The blue dotted lines represent the spheroid edge and approximate maximum penetration depth of IOAuNSs, used to calculate the bottom graph. Scale bar: 200 μm.
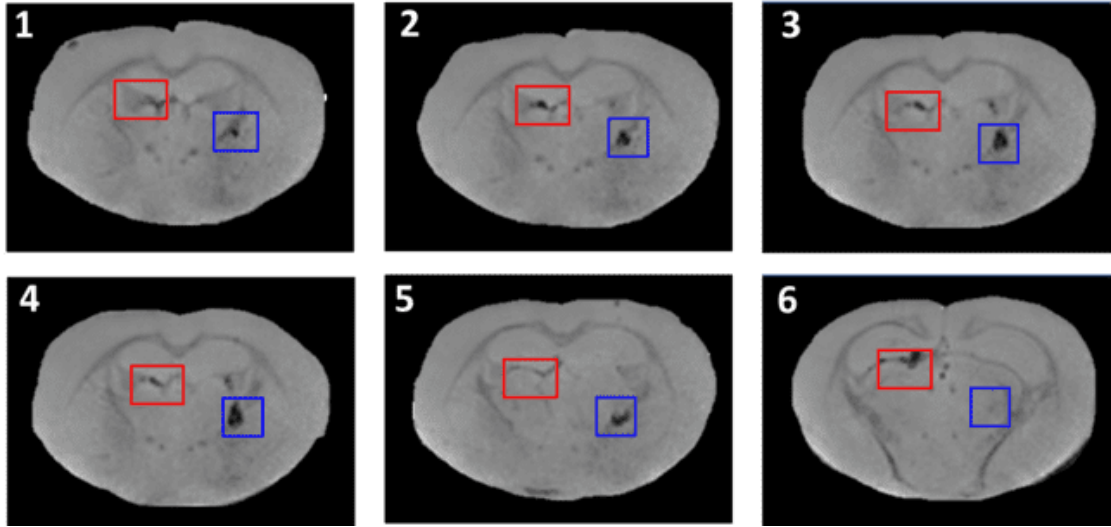
Figure S22. MRI of consecutive brain slices after injection of cells incubated with IOAuNS@2-NAT@DY633 (right hemisphere; shown by blue boxes) and IOAuNS@2-NAT@DY633 (left hemisphere; shown by red boxes). PBS buffer was injected as control (top part of both left and right hemispheres).

References

(1) Jimenez de Aberasturi, D.; Serrano-Montes, A. B.; Langer, J.; Henriksen-Lacey, M.; Parak, W. J.; Liz-Marzán, L. M. Surface Enhanced Raman Scattering Encoded Gold Nanostars for Multiplexed Cell Discrimination. *Chem. Mater.* **2016**, *28*, 6779–6790.

(2) Jimenez de Aberasturi, D.; Henriksen-Lacey, M.; Litti, L.; Langer, J.; Liz-Marzán, L. M. Using SERS Tags to Image the Three-Dimensional Structure of Complex Cell Models. *Adv. Funct. Mater.* **2020**, *30*, 1909655.

(3) Brown, A. P.; Hillier, S.; Brydson, R. M. D. Quantification of Fe-Oxidation State in Mixed Valence Minerals: A Geochemical Application of EELS Revisited. *J. Phys. Conf. Ser.* **2017**, *902* (012016).

(4) El-Khoury, P. Z.; Hu, D.; Apkarian, V. A.; Hess, W. P. Raman Scattering at Plasmonic Junctions Shorted by Conductive Molecular Bridges. *Nano Lett.* **2013**, *13*, 1858–1861.

(5) Kalbacova, J.; Rodriguez, R. D.; Desale, V.; Schneider, M.; Amin, I.; Jordan, R.; Zahn, D. R. T. Chemical Stability of Plasmon-Active Silver Tips for Tip-Enhanced Raman Spectroscopy. *Nanospectroscopy* **2015**, *1*, 12–18.

(6) Alvarez-Puebla, R. A.; Dos Santos, D. S.; Aroca, R. F. Surface-Enhanced Raman Scattering for Ultrasensitive Chemical Analysis of 1 and 2-Naphthalenethiols. *Analyst* **2004**, *129*, 1251–1256.